Gravitational wave extraction in simulations of rotating stellar core collapse

C. Reisswig,[1,*] C. D. Ott,[1,2,†] U. Sperhake,[3,1,4,‡] and E. Schnetter[2,5,6,§]

[1]*TAPIR, MC 350-17, California Institute of Technology, 1200 East California Boulevard, Pasadena, California 91125, USA*
[2]*Center for Computation and Technology, Louisiana State University, 216 Johnston Hall, Baton Rouge, Louisiana 70803, USA*
[3]*Institut de Ciències de l'Espai (CSIC-IEEC), Facultat de Ciències, Campus UAB, E-08193 Bellaterra, Spain*
[4]*Department of Physics and Astronomy, The University of Mississippi, University, Mississippi 38677-1848, USA*
[5]*Department of Physics and Astronomy, Louisiana State University, 202 Nicholson Hall, Baton Rouge, Louisiana 70803, USA*
[6]*Perimeter Institute, 31 Caroline Street North, Waterloo, Ontario N2L 2Y5, Canada*

(Received 2 December 2010; published 8 March 2011)

We perform simulations of general relativistic rotating stellar core collapse and compute the gravitational waves (GWs) emitted in the core-bounce phase of three representative models via multiple techniques. The simplest technique, the quadrupole formula (QF), estimates the GW content in the spacetime from the mass-quadrupole tensor only. It is strictly valid only in the weak-field and slow-motion approximation. For the first time, we apply GW extraction methods in core collapse that are fully curvature based and valid for strongly radiating and highly relativistic sources. These techniques are not restricted to weak-field and slow-motion assumptions. We employ three extraction methods computing (i) the Newman-Penrose (NP) scalar Ψ_4, (ii) Regge-Wheeler-Zerilli-Moncrief master functions, and (iii) Cauchy-characteristic extraction (CCE) allowing for the extraction of GWs at future null infinity, where the spacetime is asymptotically flat and the GW content is unambiguously defined. The latter technique is the only one not suffering from residual gauge and finite-radius effects. All curvature-based methods suffer from strong nonlinear drifts. We employ the fixed-frequency integration technique as a high-pass waveform filter. Using the CCE results as a benchmark, we find that finite-radius NP extraction yields results that agree nearly perfectly in phase, but differ in amplitude by $\sim$1%–7% at core bounce, depending on the model. Regge-Wheeler-Zerilli-Moncrief waveforms, while, in general, agreeing in phase, contain spurious high-frequency noise of comparable amplitudes to those of the relatively weak GWs emitted in core collapse. We also find remarkably good agreement of the waveforms obtained from the QF with those obtained from CCE. The results from QF agree very well in phase and systematically underpredict peak amplitudes by $\sim$5%–11%, which is comparable to the NP results and is certainly within the uncertainties associated with core collapse physics.

DOI: 10.1103/PhysRevD.83.064008 PACS numbers: 04.25.D−, 02.70.Bf, 04.30.Db, 97.60.Bw

I. INTRODUCTION

Massive stars ($M \gtrsim 8$–$10M_\odot$) end their nuclear burning lives with a core composed primarily of iron-group nuclei embedded in an onion-skin structure of progressively lighter elements. Energy generation has ceased in such a star's high-density core, and relativistically degenerate electrons provide pressure support against gravity. Silicon shell burning, neutrino cooling, and deleptonization eventually push the core over its effective Chandrasekhar mass. Radial instability sets in, leading to core collapse, accelerated by electron capture and photodisintegration of iron-group nuclei (see, e.g., [1,2]).

The collapsing iron core separates into a subsonically collapsing homologous ($v \propto r$) inner core and supersonically infalling outer core. When the former reaches nuclear density, the nuclear equation of state (EOS) stiffens, dramatically increasing central pressure support and stabilizing the inner core, which, due to its large inertia, overshoots its new equilibrium and then rebounds into the still collapsing outer core, launching the hydrodynamic supernova shock. The acceleration experienced by the inner core in this *core bounce* is tremendous, leading to the reversal of the collapse velocities of order $0.1c$ of its $\sim 0.5M_\odot$ of material on a millisecond time scale.

It was realized early on that the large accelerations encountered in stellar collapse, in combination with a source of quadrupole (or higher) order asphericity, lead to the emission of a burst of gravitational waves (GWs; see [3] for a historical overview). Rotation, centrifugally deforming the inner core to an oblate shape, is an obvious source of such quadrupole asymmetry, and rotating core collapse and bounce is the most extensively studied GW emission process in stellar collapse (see, e.g., [4–9] for recent studies, and references therein). Alternatively, asymmetries in collapse may arise from perturbations, e.g., due to large convective plumes in the final phase of core nuclear burning, and may lead to GW emission at bounce and/or seed GW-emitting prompt postbounce convection [3,10,11]. A multitude of GW emission processes

*reisswig@tapir.caltech.edu
†cott@tapir.caltech.edu
‡sperhake@tapir.caltech.edu
§schnetter@cct.lsu.edu

may be active in the postbounce, pre-explosion phase. These include convection/turbulence in the protoneutron star and in the postshock region, nonaxisymmetric rotational instabilities of the protoneutron star, protoneutron star pulsations, instabilities of the standing accretion shock, and asymmetric emission of neutrinos (see [3,12–16] and references therein).

Of the entire ensemble of potential GW emission processes in stellar collapse, rotating core collapse and bounce is arguably the simplest and yields the cleanest signal, depending only on rotation, on the nuclear EOS, and on the mass of the inner core at bounce [5]. Moreover, 3D studies have shown that collapsing iron cores with rotation rates in the range of what is physically plausible stay axisymmetric throughout the collapse phase and develop nonaxisymmetric dynamics only after bounce [4,6,17]. Hence, the GW signal of rotating core collapse and bounce is linearly polarized, and axisymmetric (2D) simulations are sufficient for its prediction. Unlike postbounce dynamics involving large-scale and small-scale fluid instabilities of stochastic nature, the GW signal of rotating collapse and bounce can, in principle, be predicted exactly for a given set of initial data. Hence, it has the potential of being used in GW searches using matched-filtering techniques (e.g., [18]) or alternative approaches also taking into account detailed signal predictions [19,20].

Much progress has been made in recent years in the modeling of rotating core collapse and its GW signature. State-of-the-art simulations are general relativistic (GR) [4,5,17,21–27], and some studies include magnetic fields [24,26,28] or finite-temperature EOS, deleptonization, and progenitors from stellar evolutionary calculations [4,5,25,27]. These improvements in the physics included in core collapse models provide for a more accurate and reliable dynamics underlying the emission of GWs. The calculation of the GW signal itself, however, is still being carried out predominantly in the slow-motion, weak-field quadrupole approximation (e.g., [29]) that is of questionable quality, given the extreme densities and velocities involved in core collapse. The quadrupole formula (QF) ''extracts'' GWs based on matter dynamics alone, is not invariant under general relativistic gauge transformations, treats the emission region as a point source, and suffers from the fact that the definition of the generalized mass-quadrupole moment is not unique in GR.

In GR, the GW content of a spacetime can be extracted by means of the perturbative Regge-Wheeler-Zerilli-Moncrief (RWZM) formalism [30–33], which is gauge invariant to first order, or via the Newman-Penrose (NP) scalars approach [34,35], which depends on the nonunique choice of the tetrad in which the Newman-Penrose scalars are evaluated. For reliable results, both RWZM and NP require extraction in the wave zone [29] at coordinate radii many wavelengths from the source, but even there, coordinate ambiguities exist. The latter are removed only when GWs are extracted at future null infinity ($\mathcal{J}^+$; see [34,35]), where space is asymptotically flat.

Shibata and Sekiguchi [36] have used simulations of an oscillating polytropic neutron star model to compare QF and finite-radius RWZM results. For the same basic system, Baiotti *et al.* [37] compared QF, finite-radius RWZM, and finite-radius NP GW extraction with each other and with results from a 1D perturbation analysis. Both studies found that in the context of neutron star oscillations, the *phase* of the waveforms obtained with the quadrupole approximation agrees exceptionally well with that of the RWZM and NP extraction methods. Shibata and Sekiguchi, using their particular choice of the generalized quadrupole moment, found a systematic $\sim$20% underprediction of the GW *amplitudes* by the QF. Baiotti *et al.* [37], who studied multiple incarnations of the QF, found either underprediction or overprediction of the amplitude, both by up to $\sim$60%, depending on the particular choice of QF. Nagar *et al.* [38] studied the performance of RWZM and QF-based GW extraction from oscillating polytropic tori and found qualitatively similar results, and quantitative differences in amplitudes and integrated emitted energies E_{GW} between $\sim$2% and $\sim$25%, again depending on the choice of quadrupole moment.

RWZM and NP GW extraction and comparisons with the QF approximation for GWs emitted in core collapse spacetimes have proven difficult. On the one hand, the emitted GWs are weak: Typical strain amplitudes are $Dh \sim$ 10–1000 cm, where D is the distance to the source, and typical emitted energies are of order 10^{-10}–$10^{-8} M_\odot c^2$ [3], many orders of magnitude lower than what is expected, for example, from double neutron star coalescence [39] or binary black hole mergers [40,41]. On the other hand, the GWs have typical frequencies of 100–1000 Hz and corresponding wavelengths of 300–3000 km, and hence require extraction at large coordinate radii where the grid resolution of core collapse simulations is typically too low to allow extraction of the relatively low-amplitude GWs emitted in core collapse (see, e.g., the discussion in [42]). Shibata and Sekiguchi, in [17], were able to extract GWs with the RWZM formalism from an extreme core collapse model that developed a rotationally induced large-scale nonaxisymmetric deformation after bounce, emitting GWs with $Dh \sim 20\,000$ cm. For this model, they found that the QF accurately predicts the GW phase, but underestimates the strain amplitude by $\sim$10%. Because of the aforementioned difficulties, these authors were unable to compare RWZM with QF for more moderate, axisymmetric models. Cerdá-Durán *et al.* [43] performed core collapse simulations using a second-order post-Newtonian (2PN) extension of the conformal-flatness approximation to GR. Exploiting an approximate relationship of the nonconformal 2PN part of the metric to its GW part [43], they were able to extract GWs from their 2PN metric in standard axisymmetric rotating core collapse models.

They found very close agreement (to a few percent in strain amplitude) between QF and 2PN GW signals for almost all considered collapse models. Siebel *et al.* [44] performed nonrotating axisymmetric core collapse simulations by employing evolutions based on a fully general relativistic null cone formalism. They added nonspherical perturbations to the star, leading to the emission of GWs, which they were able to extract with the Bondi news function at $\mathcal{J}^+$. Comparisons to the QF suggested a significant discrepancy in amplitude and frequency from the more reliable Bondi news result.

The results of Shibata and Sekiguchi [17] and of Cerdá-Durán *et al.* [43] provide some handle on the performance of the QF approximation in core collapse spacetimes. The former study, while being performed in full GR, considered only a single extreme model. In addition, the authors were forced to extract GWs with RWZM at too small radii for completely reliable results. The latter study, while considering a broader ensemble of models, was restricted to 2PN without considering full GR, leaving room for doubts about the quality of their GW extraction technique. Finally, the results of Siebel *et al.* [44] were limited to axisymmetry without rotation and are unreliable in the presence of strong shocks.

In this study, we readdress GW extraction from rotating core collapse spacetimes. We perform 3 + 1 GR hydrodynamics simulations of rotating core collapse, for the first time in the core collapse context extracting GWs with RWZM, NP, and multiple QFs and comparing the results of these methods. In addition, and also for the first time in the present context, we utilize the Cauchy-characteristic extraction (CCE) approach [45–49] that propagates the GW information to $\mathcal{J}^+$ for completely gauge independent and unambiguous GW extraction.

In choosing our models set, we are guided by Cerdá-Durán *et al.* [43], and draw precollapse configurations from the set of [21]. These models are GR $n = 3$-polytropic iron cores in rotational equilibrium, and we evolve them with an analytic hybrid polytropic/Γ-law EOS used in many previous studies of rotating core collapse [17,21,23,24,28,43,50]. For physically accurate GW signal predictions to be used in GW data analysis, a microphysically more complete treatment is warranted. Fortunately, recent results of studies employing such modeling technology (e.g., [4,5,25,27,51]) show that, with a proper choice of EOS parameters, hybrid-EOS models are able to qualitatively and, to some extent, quantitatively reproduce the GW signals obtained with the much more complex and computationally intensive microphysical studies. Hence, for the purpose of this study, we resort to the simpler hybrid-EOS models.

Our simulations employ the open-source ZELMANI GR core collapse simulation package [52] that is based on the CACTUS COMPUTATIONAL TOOLKIT [53,54] and the EINSTEIN TOOLKIT [55]. While using the full 3 + 1 GR formalism, we limit our simulations to an octant of the 3D cube, using periodic boundary conditions on two of the inner faces of the octant and reflective boundary conditions on the third face. This limits the 3D structure to even ℓ and m that are multiples of 4, which is not a limitation for the current study, since rotating core collapse and the very early postbounce evolution are likely to proceed nearly axisymmetrically [4,6,56]. We note that, even though the GW signal in rotating core collapse is dominated by the ($\ell = 2$, $m = 0$) "+" polarization mode, there is no reason to expect different behavior for other GW multipoles or polarizations, and our results should translate to the nonaxisymmetric case.

The results of our simulations indicate that NP extraction yields results that agree well with those obtained from the most sophisticated CCE method. We observe differences in amplitude of 1%–7%, depending on the model, while the agreement in phase is nearly perfect. We also find that the RWZM formalism yields unphysical high-frequency signal components that make this method less suitable for core collapse simulations where the signal is very weak. Finally, we note that the quadrupole approximation yields surprisingly close results to those obtained from CCE. While the phases nearly perfectly agree, the amplitude shows differences of 5%–11%.

This paper is structured as follows. In Sec. II, we discuss our methodology, initial data, and EOS details. Section III discusses the various GW extraction methods that we employ. In Sec. IV, we present our results and discuss them in detail. Finally, in Sec. V, we summarize and review our findings.

II. METHODS

We adopt the Arnowitt-Deser-Misner (ADM) 3 + 1 foliation of spacetime [57]. All equations assume $c = G = 1$ unless noted otherwise. In the following, Latin indices run from 1 to 3 while Greek ones run from 0 to 3. We adhere to abstract index notation. $g_{\mu\nu}$ is the 4-metric, γ_{ij} is the 3-metric, and K_{ij} the extrinsic curvature.

A. Infrastructure and mesh refinement: CACTUS and CARPET

Our code uses the CACTUS COMPUTATIONAL TOOLKIT [53,54] to manage the complexity inherent in large software projects. CACTUS is an open-source high-performance computing environment designed for scientists and engineers; its modular structure enables parallel computation across different architectures, and facilitates collaborative code development between different groups. Indeed, our code uses a set of components of the public EINSTEIN TOOLKIT [55,58], a community project developing and supporting open software for relativistic astrophysics, such as e.g. the curvature and hydrodynamics evolution methods described below. Many improvements made in the

course of the research for this paper were contributed back to the community.

In particular, CACTUS allows us to clearly separate between physics components and computational components in our code. Distributed memory parallelism in CACTUS is provided by a *driver* component which implements the data structures discretizing the manifold on which the computational state vector lives. In our case, this is the CARPET driver [59–61] providing block-structured adaptive mesh refinement (AMR) and multiblock discretization. CARPET parallelizes using a hybrid approach combining MPI and OPENMP, where internode communication is handled via MPI and intranode communication via OPENMP or via MPI, depending on the particular system and on details of the simulation setup.

CARPET implements Berger-Oliger–style AMR [62], where the fine grids are aligned with coarse grids, refined by factors of 2. CARPET also implements subcycling in time, where finer grids take two time steps for every coarse grid step. The latter greatly improves efficiency, but also introduces significant complexity into the time evolution method. The refined regions can be chosen and modified arbitrarily, which we use here to add additional, finer levels during evolution, as successively higher resolutions are required to capture the collapse. This is described in more detail in [42].

We use fifth-order accurate spatial interpolation for spacetime variables and third-order essentially nonoscillatory interpolation for hydrodynamics variables. Time interpolation, which is necessary to provide boundary conditions to fine levels at times where there is no coarse level, is second-order accurate. We apply no time refinement between levels 3 and 4, which corresponds to reducing the Courant-Friedrichs-Lewy factor on levels 3 and coarser by a factor of 2. This increases the accuracy on level 3, where we extract gravitational waves. In total, we use nine refinement levels (including the base grid), an outer boundary radius of $3840M_\odot$ (~ 5700 km), and a finest zone size of $0.25M_\odot$ (~ 370 m) in our baseline resolution.

B. Curvature evolution: MCLACHLAN

1. Evolution system

We evolve the full Einstein equations in a 3 + 1 split (a Cauchy initial boundary value problem) [63], using the Baumgarte-Shapiro-Shibata-Nakamura (BSSN) formulation [64], a 1 + log slicing [65], and a Γ-driver shift condition [65]. This leads to the following set of evolved variables:

$$\phi := \log\left[\frac{1}{12}\det\gamma_{ij}\right], \tag{1}$$

$$\tilde{\gamma}_{ij} := e^{-4\phi}\gamma_{ij}, \tag{2}$$

$$K := g^{ij}K_{ij}, \tag{3}$$

$$\tilde{A}_{ij} := e^{-4\phi}[K_{ij} - \tfrac{1}{3}g_{ij}K], \tag{4}$$

$$\tilde{\Gamma}^i := \tilde{\gamma}^{jk}\tilde{\Gamma}^i_{jk}. \tag{5}$$

Our exact evolution equations are as described by Eqs. (3)–(10) of [66], which we list here for completeness:

$$\partial_0\alpha = -\alpha^2 f(\alpha, \phi, x^\mu)(K - K_0(x^\mu)), \tag{6}$$

$$\partial_0 K = -e^{-4\phi}[\tilde{D}^i\tilde{D}_i\alpha + 2\partial_i\phi\cdot\tilde{D}^i\alpha] + \alpha(\tilde{A}^{ij}\tilde{A}_{ij} + \tfrac{1}{3}K^2) - \alpha S, \tag{7}$$

$$\partial_0\beta^i = \alpha^2 G(\alpha, \phi, x^\mu)B^i, \tag{8}$$

$$\partial_0 B^i = e^{-4\phi}H(\alpha, \phi, x^\mu)\partial_0\tilde{\Gamma}^i - \eta^i(B^i, \alpha, x^\mu), \tag{9}$$

$$\partial_0\phi = -\frac{\alpha}{6}K + \frac{1}{6}\partial_k\beta^k, \tag{10}$$

$$\partial_0\tilde{\gamma}_{ij} = -2\alpha\tilde{A}_{ij} + 2\tilde{\gamma}_{k(i}\partial_{j)}\beta^k - \tfrac{2}{3}\tilde{\gamma}_{ij}\partial_k\beta^k, \tag{11}$$

$$\partial_0\tilde{A}_{ij} = e^{-4\phi}[\alpha\tilde{R}_{ij} + \alpha R^\phi_{ij} - \tilde{D}_i\tilde{D}_j\alpha + 4\partial_{(i}\phi\cdot\tilde{D}_{j)}\alpha]^{\mathrm{TF}} + \alpha K\tilde{A}_{ij} - 2\alpha\tilde{A}_{ik}\tilde{A}^k_j + 2\tilde{A}_{k(i}\partial_{j)}\beta^k - \tfrac{2}{3}\tilde{A}_{ij}\partial_k\beta^k - \alpha e^{-4\phi}\hat{S}_{ij}, \tag{12}$$

$$\partial_0\tilde{\Gamma}^i = \tilde{\gamma}^{kl}\partial_k\partial_l\beta^i + \frac{1}{3}\tilde{\gamma}^{ij}\partial_j\partial_k\beta^k + \partial_k\tilde{\gamma}^{kj}\cdot\partial_j\beta^i - \frac{2}{3}\partial_k\tilde{\gamma}^{ki}\cdot\partial_j\beta^j - 2\tilde{A}^{ij}\partial_j\alpha + 2\alpha\Big[(m-1)\partial_k\tilde{A}^{ki} - \frac{2m}{3}\tilde{D}^i K + m(\tilde{\Gamma}^i_{kl}\tilde{A}^{kl} + 6\tilde{A}^{ij}\partial_j\phi)\Big] - S^i, \tag{13}$$

with the momentum constraint damping constant set to $m = 1$. The stress-energy tensor $T_{\mu\nu}$ is incorporated via the projections

$$\rho := \frac{1}{\alpha^2}(T_{00} - 2\beta^i T_{0i} + \beta^i\beta^j T^{ij}), \tag{14}$$

$$S := g^{ij}T_{ij}, \tag{15}$$

$$S_i := -\frac{1}{\alpha}(T_{0i} - \beta^j T_{ij}). \tag{16}$$

We have introduced the notation $\partial_0 = \partial_t - \beta^j\partial_j$. All quantities with a tilde refer to the conformal 3-metric $\tilde{\gamma}_{ij}$, which is used to raise and lower indices. In particular, $\tilde{D}_i$ and $\tilde{\Gamma}^k_{ij}$ refer to the covariant derivative and the Christoffel symbols with respect to $\tilde{\gamma}_{ij}$. The expression $[\cdots]^{\mathrm{TF}}$ denotes the trace-free part of the expression inside the parentheses, and we define the Ricci tensor contributions

$$\tilde{R}_{ij} = -\tfrac{1}{2}\tilde{\gamma}^{kl}\partial_k\partial_l\tilde{\gamma}_{ij} + \tilde{\gamma}_{k(i}\partial_{j)}\tilde{\Gamma}^k - \tilde{\Gamma}_{(ij)k}\partial_l\tilde{\gamma}^{lk} + \tilde{\gamma}^{ls}(2\tilde{\Gamma}^k_{l(i}\tilde{\Gamma}_{j)ks} + \tilde{\Gamma}^k_{is}\tilde{\Gamma}_{klj}), \tag{17}$$

$$R^\phi_{ij} = -2\tilde{D}_i\tilde{D}_j\phi - 2\tilde{\gamma}_{ij}\tilde{D}^k\tilde{D}_k\phi + 4\tilde{D}_i\phi\tilde{D}_j\phi - 4\tilde{\gamma}_{ij}\tilde{D}^k\phi\tilde{D}_k\phi. \tag{18}$$

This is a so-called ϕ variant of the BSSN formulation. The evolved gauge variables are lapse α, shift β^i, and a

quantity B^i related to the time derivative of the shift. The gauge parameters f, G, H, and η are determined by our choice of a 1 + log slicing:

$$f(\alpha, \phi, x^\mu) := 2/\alpha, \tag{19}$$

$$K_0(x^\mu) := 0, \tag{20}$$

and Γ-driver shift condition:

$$G(\alpha, \phi, x^\mu) := (3/4)\alpha^{-2}, \tag{21}$$

$$H(\alpha, \phi, x^\mu) := \exp\{4\phi\}, \tag{22}$$

$$\eta(B^i, \alpha, x^\mu) := (1/2)B^i q(r). \tag{23}$$

The expression $q(r)$ attenuates the Γ driver, depending on the radius as described below.

The Γ-driver shift condition is symmetry seeking, driving the shift β^i to a state that renders the conformal connection functions $\tilde{\Gamma}^i$ stationary. Of course, such a stationary state cannot be achieved while the metric is evolving, but in a stationary spacetime the time evolution of the shift β^i and thus that of the spatial coordinates x^i will be exponentially damped. This damping time scale is set by the gauge parameter η [see Eq. (23)] which has dimension $1/T$ (inverse time). As described, e.g., in [67,68], this time scale may need to be adapted in different regions of the domain to avoid spurious high-frequency behavior in regions that otherwise evolve only very slowly, e.g., far away from the source.

Here we use the simple damping mechanism described in Eq. (12) of [68], which is defined as

$$q(r) := \begin{cases} 1 & \text{for } r \le R \text{ (near the origin)} \\ R/r & \text{for } r \ge R \text{ (far away)}, \end{cases} \tag{24}$$

with a constant R defining the transition radius between the interior, where $q \approx 1$, and the exterior, where q falls off as $1/r$. Equation (23) describes how q appears in the gauge parameters. In this paper we use $R = 250M_\odot$ ($R = 369.2$ km).

We implement the above BSSN equations and gauge conditions in the MCLACHLAN code [66,69], which is freely available as part of the EINSTEIN TOOLKIT. MCLACHLAN is autogenerated from the definition of the variables and equations in the MATHEMATICA format by the KRANC code generator [70–72]. KRANC is a suite of MATHEMATICA packages comprising a computer algebra toolbox for numerical relativists. KRANC can be used as a "rapid prototyping" system for physicists or mathematicians handling complex systems of partial differential equations, and through integration into the CACTUS framework, one can also produce efficient production codes.

We use fourth-order accurate finite differencing for the spacetime variables and add a fifth-order Kreiss-Oliger dissipation term to remove high-frequency noise. We use a fourth-order Runge-Kutta time integrator for all evolved variables.

2. Initial conditions

We set up our initial condition from the ADM variables g_{ij}, K_{ij}, lapse α, and shift β^i, as provided by the initial data discussed in Sec. II D. From these we calculate the BSSN quantities via their definition, setting $B^i = 0$, and using cubic extrapolation for $\tilde{\Gamma}^i$ at the outer boundary. This extrapolation is necessary since the $\tilde{\Gamma}^i$ are calculated from derivatives of the metric, and one cannot use centered finite differencing stencils near the outer boundary. We assume that one could instead also use one-sided derivatives to calculate $\tilde{\Gamma}^i$ on the boundary.

The extrapolation stencils distinguish between points on the faces, edges, and corners of the grid. Points on the faces are extrapolated via stencils perpendicular to that face, while points on the edges and corners are extrapolated with stencils aligned with the average of the normals of the adjoining faces. For example, points on the $(+x, +y)$ edge are extrapolated in the (1, 1, 0) direction, while points in the $(+x, +y + z)$ corner are extrapolated in the (1, 1, 1) direction. Since several layers of boundary points have to be filled for higher-order schemes (e.g., three layers for a fourth-order scheme), we proceed outwards starting from the innermost layer. Each subsequent layer is then defined via the points in the interior and the previously calculated layers.

3. Boundary conditions

During time evolution, we apply a Sommerfeld-type radiative boundary condition to all components of the evolved BSSN variables as described in [64]. The main feature of this boundary condition is that it assumes approximate spherical symmetry of the solution, while applying the actual boundary condition on the boundary of a cubic grid where the face normals are not aligned with the radial direction. This boundary condition defines the right-hand side of the BSSN state vector on the outer boundary, which is then integrated in time as well, so that the boundary and interior are calculated with the same order of accuracy.

The main part of the boundary condition assumes that we have an outgoing radial wave with some speed v_0:

$$X = X_0 + \frac{u(r - v_0 t)}{r}, \tag{25}$$

where X is any of the tensor components of evolved variables, X_0 the value at infinity, and u a spherically symmetric perturbation. Both X_0 and v_0 depend on the particular variable and have to be specified. This implies the following differential equation:

$$\partial_t X = -v^i \partial_i X - v_0 \frac{X - X_0}{r}, \tag{26}$$

where $v^i = v_0 x^i / r$. The spatial derivatives ∂_i are evaluated using centered finite differencing where possible, and

one-sided finite differencing elsewhere. We use second-order stencils in our implementation.

In addition to this main part, we also account for those parts of the solution that do not behave as a pure wave, e.g., Coulomb-type terms caused by infall of the coordinate lines. We assume that these parts decay with a certain power p of the radius. We implement this by considering the radial derivative of the source term above, and extrapolating according to this power-law decay.

Given a source term $(\partial_t X)$, we define the corrected source term $(\partial_t X)^*$ via

$$(\partial_t X)^* = (\partial_t X) + \left(\frac{r}{r - n^i \partial_i r}\right)^p n^i \partial_i (\partial_t X), \tag{27}$$

where n^i is the normal vector of the corresponding boundary face. The spatial derivatives ∂_i are evaluated by comparing neighboring grid points, corresponding to a second-order stencil evaluated in the middle between the two neighboring grid points. We assume a second-order decay; i.e., we choose $p = 2$.

As with the initial conditions above, this boundary condition is evaluated on several layers of grid points, starting from the innermost layer. Both the extrapolation and radiative boundary condition algorithms are implemented in the publicly available NEWRAD component of the EINSTEIN TOOLKIT.

This boundary condition is only a coarse approximation of the actual decay behavior of the BSSN state vector, and it does not capture the correct behavior of the evolved variables. However, we observe that this boundary condition leads to stable evolutions if applied sufficiently far from the source. Errors introduced at the boundary (both errors in the geometry and constraint violations) propagate inwards with the speed of light [66]. Gauge changes introduced by the boundary condition, which are physically not observable, propagate faster, with a speed up to $\sqrt{2}$ for our gauge conditions.

C. General relativistic hydrodynamics: GRHYDRO

We employ the open-source GR hydrodynamics code GRHYDRO that is part of the EINSTEIN TOOLKIT [55] and is an updated version of the code WHISKY described in [73].

The equations of ideal GR hydrodynamics evolved by GRHYDRO are derived from the local GR conservation laws of mass and energy-momentum,

$$\nabla_\mu J^\mu = 0, \qquad \nabla_\mu T^{\mu\nu} = 0, \tag{28}$$

where ∇_μ denotes the covariant derivative with respect to the 4-metric. $J^\mu = \rho u^\mu$ is the mass current with the 4-velocity u^μ and the rest-mass density ρ. $T^{\mu\nu} = \rho h u^\mu u^\nu + P g^{\mu\nu}$ is the stress-energy tensor. The quantity $h = 1 + \epsilon + P/\rho$ is the specific enthalpy, P is the fluid pressure, and ϵ is the specific internal energy.

We choose a definition of the 3-velocity that corresponds to the velocity seen by an Eulerian observer at rest in the current spatial 3-hypersurface [74],

$$v^i = \frac{u^i}{W} + \frac{\beta^i}{\alpha}, \tag{29}$$

where $W = (1 - v^i v_i)^{-1/2}$ is the Lorentz factor. In terms of the 3-velocity, the contravariant 4-velocity is then given by

$$u^0 = \frac{W}{\alpha}, \qquad u^i = W\left(v^i - \frac{\beta^i}{\alpha}\right), \tag{30}$$

and the covariant 4-velocity is

$$u_0 = W(v^i \beta_i - \alpha), \qquad u_i = W v_i. \tag{31}$$

The GRHYDRO scheme is written in a first-order hyperbolic flux-conservative evolution system for the conserved variables $\hat{D}$, $\hat{S}^i$, and $\hat{\tau}$ in terms of the primitive variables ρ, ϵ, v^i,

$$\begin{aligned} \hat{D} &= \sqrt{\gamma}\rho W, \qquad \hat{S}^i = \sqrt{\gamma}\rho h W^2 v^i, \\ \hat{\tau} &= \sqrt{\gamma}(\rho h W^2 - P) - D, \end{aligned} \tag{32}$$

where γ is the determinant of γ_{ij}. The evolution system then becomes

$$\frac{\partial \mathbf{U}}{\partial t} + \frac{\partial \mathbf{F}^i}{\partial x^i} = \mathbf{S}, \tag{33}$$

with

$$\begin{aligned} &\mathbf{U} = [\hat{D}, \hat{S}_j, \hat{\tau}], \\ &\mathbf{F}^i = \alpha[\hat{D}\tilde{v}^i, \hat{S}_j \tilde{v}^i + \delta^i_j P, \hat{\tau}\tilde{v}^i + P v^i], \\ &\mathbf{S} = \alpha\left[0, T^{\mu\nu}\left(\frac{\partial g_{\nu j}}{\partial x^\mu} - \Gamma^\lambda_{\mu\nu} g_{\lambda j}\right), \alpha\left(T^{\mu 0}\frac{\partial \ln\alpha}{\partial x^\mu} - T^{\mu\nu}\Gamma^0_{\mu\nu}\right)\right]. \end{aligned} \tag{34}$$

Here, $\tilde{v}^i = v^i - \beta^i/\alpha$ and $\Gamma^\lambda_{\mu\nu}$ are the 4-Christoffel symbols. The above equations are solved in a semidiscrete fashion. The spatial discretization is performed by means of a high-resolution shock-capturing (HRSC) scheme employing a second-order accurate finite-volume discretization. We make use of the Marquina flux formula for the local Riemann problems and piecewise-parabolic cell interface reconstruction (PPM). For a review of such methods in the GR context, see [75]. The time integration and coupling with curvature are carried out with the Method of Lines [76].

D. Equation of state and initial stellar models

For the purpose of this study, we employ the simple analytic *hybrid* EOS [21,77] that combines a two-piece piecewise polytropic pressure $P_{\rm P}$ with a thermal component $P_{\rm th}$, i.e., $P = P_{\rm P} + P_{\rm th}$. To model the stiffening of the EOS at nuclear density $\rho_{\rm nuc} \cong 2 \times 10^{14}\ {\rm g\,cm^{-3}}$, we

assume that the polytropic index γ jumps from γ_1 below nuclear density to γ_2 above. As detailed in [78], it is possible to construct an EOS that is continuous at $\rho_{\rm nuc}$,

$$P = \frac{\gamma - \gamma_{\rm th}}{\gamma - 1} K \rho_{\rm nuc}^{\gamma_1 - \gamma} \rho^{\gamma} - \frac{(\gamma_{\rm th} - 1)(\gamma - \gamma_1)}{(\gamma_1 - 1)(\gamma_2 - 1)} K \rho_{\rm nuc}^{\gamma_1 - 1} \rho + (\gamma_{\rm th} - 1)\rho\epsilon. \quad (35)$$

In this, $\epsilon = \epsilon_{\rm P} + \epsilon_{\rm th}$ denotes the total specific internal energy which consists of a polytropic and a thermal contribution. $K = 4.897 \times 10^{14}$ (cgs) is the polytropic constant for a polytrope of relativistic degenerate electrons at $Y_e = 0.5$. The thermal index $\gamma_{\rm th} = 1.5$ corresponds to a mixture of relativistic ($\gamma = 4/3$) and nonrelativistic ($\gamma = 5/3$) gas. This EOS mimics the effects of the stiffening of the physical EOS at $\rho_{\rm nuc}$ and can handle the significant thermal pressure contribution introduced by shock heating in the postbounce phase. Provided appropriate choices of EOS parameters (e.g., [27]), the hybrid EOS leads to qualitatively correct collapse and bounce dynamics. Consequently, this leads to GW signals that are similar in morphology, characteristic frequencies, and amplitudes to those computed from more microphysically complete simulations [4,5,51].

We employ $n = 3$ ($\gamma_{\rm ini} = \gamma = 4/3$) polytropes in rotational equilibrium generated via Hachisu's self-consistent field method [79,80] that not only provides fluid, but also spacetime curvature initial data. The polytropes are set up with the rotation law discussed in [21,50] and are parametrized via the differential rotation parameter A and the initial ratio $T/|W|$ of rotational kinetic energy T to gravitational binding energy $|W|$. While being set up as marginally stable polytropes with $\gamma_{\rm ini} = 4/3$, during evolution, the initial subnuclear polytropic index γ_1 is reduced to $\gamma_1 < \gamma_{\rm ini}$ to accelerate collapse. Following previous studies [21,25,50], we use $\gamma_2 = 2.5$ in the supernuclear regime.

From the initial stellar configurations of [21,50] we draw a subset of three models that cover the range of astrophysically expected GW signals from rotating iron core collapse [5] and accretion-induced collapse [51]. Our choices have been used previously in a comparison study of full GR and conformally flat simulations [25]:

(i) Model A1B3G3 is in near uniform rotation with $A = 50 \times 10^3$ km, has $T/|W| = 0.9\%$, and, once mapped to the evolution grid, uses a subnuclear adiabatic index $\gamma_1 = 1.31$. Its GW signal is of the standard "type I" morphology [21,27,50] and of moderate strength (see [21,25] for details).

(ii) Model A3B3G3 also uses $\gamma_1 = 1.31$. It is strongly differentially rotating, with its initial central angular velocity dropping by a factor of 2 over $A = 500$ km. This, in combination with $T/|W| = 0.9\%$, leads to rapid rotation in the inner core, resulting in a very strong GW signal at core bounce and dynamics that are significantly affected by centrifugal effects. It produces a type I GW signal with a centrifugally widened broad peak at core bounce.

(iii) Model A1B3G5 has the same rotational setup as model A1B3G3, but its subnuclear adiabatic index is reduced to $\gamma_1 = 1.28$. This leads to rapid collapse, to a very small inner core at core bounce, and to a weak "type III" GW signal [21,50] akin to that potentially emitted by an accretion-induced collapse event [51].

TABLE I. Initial parameters of differentially rotating stellar cores used for the core collapse simulations. The models are described by three quantities: the degree of differential rotation A, the ratio $T/|W|$ of rotational to potential energy, and the subnuclear adiabatic index γ_1 during the collapse. For convenience, we also report the wave-signature type of the three models and the mass M present on the computational grid.

Model	Type	A (10^3 km)	$T/\lvert W\rvert$ (%)	γ_1	M ($M_\odot$)
A1B3G3	I (weak)	50.0	0.89	1.31	1.46
A1B3G5	III	50.0	0.89	1.28	1.46
A3B3G3	I (strong)	0.5	0.89	1.31	1.46

For convenience, key model parameters are summarized in Table I.

III. GRAVITATIONAL WAVE EXTRACTION

A. The quadrupole approximation

The quadrupole approximation is the only means of extracting GWs in Newtonian or conformally flat GR simulations, but has found wide application also in GR simulations of stellar collapse [4,17,23,25].

The coordinate-dependent quadrupole formula estimates the GW strain seen by an asymptotic observer by considering exclusively the quadrupole stress-energy source. It neglects any nonlinear GR effects. This approximation is valid strictly only in the weak-field $\frac{G}{c^2}\frac{R}{M} \ll 1$ and slow-motion $\frac{v}{c} \ll 1$ limits [29], where spacetime is essentially flat.

The quadrupole formula is given in the transverse-traceless (TT) gauge by

$$h_{jk}^{TT}(t, \mathbf{x}) = \frac{2}{c^4}\frac{G}{R}\left[\frac{d^2}{dt^2} I_{jk}(t - R/c)\right]^{TT}, \quad (36)$$

where

$$I_{jk} = \int \tilde{\rho}(t, \mathbf{x})\left[x_j x_k - \frac{1}{3}x^2 \delta_{jk}\right] d^3x \quad (37)$$

denotes the reduced mass-quadrupole tensor. Since we are working in the weak-field, slow-motion approximation, the placement of tensor indices is arbitrary. I_{jk} is not uniquely defined in GR, and the choice of the density variable $\tilde{\rho}$ is not obvious. Following [4,5,21,23,25], we set $\tilde{\rho} = \sqrt{\gamma} W \rho = \hat{D}$, because (i) this is the conserved density

variable in our code, and (ii) $\sqrt{\gamma}d^3x$ is the natural volume element. See [37] for other potential choices and their relative performance for GWs from oscillating polytropes.

The reduced mass-quadrupole tensor can be computed directly from the computed distribution $\hat{D}(t, \mathbf{x})$. In order to eliminate the effects of numerical noise when differentiating Eq. (37) twice in time, we make use of the continuity equation to obtain the first time derivative of Eq. (37) without numerical differentiation [22,81,82],

$$\frac{d}{dt}I_{jk} = \int \hat{D}(t, \mathbf{x})\left[\tilde{v}^j x^k + \tilde{v}^k x^j - \frac{2}{3}(x^l \tilde{v}^l)\delta^{jk}\right]d^3x, \quad (38)$$

where we set $\tilde{v}^i = v^i$ as defined by Eq. (29). Note that we have switched to contravariant variables in the integrand, as these are the ones present in the code. Finally, the remaining time derivative needed for evaluating the quadrupole GW strain [Eq. (36)] is performed numerically.

In order to assess the sensitivity of the predicted waves on the particular choice of the velocity variable $\tilde{v}^i$ in Eq. (38), we implement two modified versions. In variant VS, we use Shibata *et al.*'s definition of the 3-velocity (e.g., [23]) that differs from ours by a gauge term. In variant PV, we follow [78] and employ physical velocity components (individually bound to $v < c$) that, in Cartesian coordinates, are given by $\{v_x, v_y, v_z\} \approx \{\sqrt{\gamma_{11}}v^1, \sqrt{\gamma_{22}}v^2, \sqrt{\gamma_{33}}v^3\}$, assuming that the 3-metric is nearly diagonal (which is the case in our gauge; see Sec. II B).

B. The Regge-Wheeler-Zerilli-Moncrief formalism

A particular *Ansatz* for analyzing gravitational radiation in terms of odd and even multipoles in the far field of the source was originally developed by Regge, Wheeler [30], and Zerilli [31,32], respectively. Moncrief subsequently provided a gauge-invariant reformulation [83] (see [84] for a review). Assuming that, at large distances from the source, the GW content of the spacetime can be viewed as a linear perturbation to a fixed background, we can write

$$g_{\mu\nu} = g^0_{\mu\nu} + h_{\mu\nu}, \quad (39)$$

where $g^0_{\mu\nu}$ is the fixed background metric and $h_{\mu\nu}$ its linear perturbation. The background metric $g^0_{\mu\nu}$ is usually assumed to be of Minkowski or Schwarzschild form, which we can write as

$$ds^2 = -Ndt^2 + Adr^2 + r^2(d\theta^2 + \sin^2\theta d\phi^2). \quad (40)$$

By splitting the spacetime into timelike and radial and angular parts, it is possible to decompose the metric perturbation $h_{\mu\nu}$ into odd and even multipoles; i.e., we can write

$$h_{\mu\nu} = \sum_{\ell m}[(h^{\ell m}_{\mu\nu})^{(o)} + (h^{\ell m}_{\mu\nu})^{(e)}]. \quad (41)$$

The even and odd multipole components are defined according to their behavior under a parity transformation $(\theta, \phi) \to (\pi - \theta, \pi + \phi)$. Odd multipoles transform as $(-1)^{\ell+1}$ while even multipoles transform as $(-1)^{\ell}$. Both multipole components can be expanded in terms of vector and tensor spherical harmonics (e.g., [29]).

Given the Hamiltonian of the perturbed Einstein equations in ADM form [85], it is then possible to derive variational principles for the odd- and even-parity perturbations [83] to give equations of motion that are similar to wave equations with a scattering potential.

The solutions to the odd- and even-parity wave equations are given by the Regge-Wheeler-Moncrief and the Zerilli-Moncrief master functions, respectively. The odd-parity Regge-Wheeler-Moncrief function reads

$$Q^{\times}_{\ell m} \equiv \sqrt{\frac{2(\ell+1)!}{(\ell-2)!}}\frac{1}{r}\left(1 - \frac{2M}{r}\right) \times \left[(h^{\ell m}_1)^{(o)} + \frac{r^2}{2}\partial_r\left(\frac{(h^{\ell m}_2)^{(o)}}{r^2}\right)\right], \quad (42)$$

and the even-parity Zerilli-Moncrief function reads

$$Q^{+}_{\ell m} \equiv \sqrt{\frac{2(\ell+1)!}{(\ell-2)!}}\frac{rq^{\ell m}_1}{\Lambda[r(\Lambda-2)+6M]}, \quad (43)$$

where $\Lambda = \ell(\ell+1)$, and where

$$q^{\ell m}_1 \equiv r\Lambda\kappa^{\ell m}_1 + \frac{4r}{A^2}\kappa^{\ell m}_2, \quad (44)$$

with

$$\kappa^{\ell m}_1 \equiv K^{\ell m} + \frac{1}{A}\left(r\partial_r G^{\ell m} - \frac{2}{r}(h^{\ell m}_1)^{(e)}\right), \quad (45)$$

$$\kappa^{\ell m}_2 \equiv \tfrac{1}{2}[AH^{\ell m}_2 - \sqrt{A}\partial_r(r\sqrt{A}K^{\ell m})]. \quad (46)$$

These master functions depend entirely on the spherical part of the metric given by the coefficients N and A, and the perturbation coefficients for the individual metric perturbation components $(h^{\ell m}_1)^{(o)}$, $(h^{\ell m}_2)^{(o)}$, $(h^{\ell m}_1)^{(e)}$, $(h^{\ell m}_2)^{(e)}$, $H^{\ell m}_0$, $H^{\ell m}_1$, $H^{\ell m}_2$, $K^{\ell m}$, and $G^{\ell m}$ which can be obtained from any numerical spacetime by projecting out the Schwarzschild or Minkowski background [86]. For example, the coefficient $H^{\ell m}_2$ can be obtained via

$$H^{\ell m}_2 = \frac{1}{A}\int (g_{rr} - A)Y_{\ell m}d\Omega, \quad (47)$$

where g_{rr} is the radial component of the numerical metric represented in the spherical-polar coordinate basis, $Y_{\ell m}$ are spherical harmonics, and $d\Omega$ is the surface line element of the S^2 extraction sphere. The coefficient A represents the spherical part of the background metric and can be obtained by projection of the numerical metric component g_{rr} on Y_{00} over the extraction sphere

$$A = \frac{1}{4\pi}\int g_{rr}d\Omega. \quad (48)$$

Similar expressions hold for the remaining perturbation coefficients.

The odd- and even-parity master functions Eqs. (42) and (43) can be straightforwardly related to the gravitational wave strain and are given by

$$h_+ - \mathrm{i}h_\times = \frac{1}{\sqrt{2}r}\sum_{\ell,m}\left(Q^+_{\ell m} - \mathrm{i}\int_{-\infty}^{t} Q^\times_{\ell m}(t')dt'\right){}_{-2}Y^{\ell m}(\theta,\phi) + \mathcal{O}\left(\frac{1}{r^2}\right), \tag{49}$$

where ${}_{-2}Y^{\ell m}(\theta,\phi)$ are the spin-weight $s=-2$ spherical harmonics. We note that this relation is strictly true only at an infinite distance from the source. Since our numerical domain is finite in size, we choose some, ideally large, but finite radius. In Sec. IV C, we check how well the GWs extracted with the RWZM formalism asymptote with increasing extraction radius.

In the present work, our models exclusively trigger the even-parity master function Q^+, and $Q^\times$ is zero. In this case, we can simplify Eq. (49) and obtain

$$h_{+,e} = \frac{1}{\sqrt{2}r} Q^+_{20}{}_{-2}Y^{20}(\theta,\phi), \tag{50}$$

relating the strain directly to Q^+.

C. Newman-Penrose scalars

Another method for calculating the gravitational waveforms is based on the conformal structure of asymptotically flat spacetimes as established by Bondi, Sachs, and Penrose [35,87,88]. This method is conveniently represented in terms of spin-weighted scalars as introduced by Newman and Penrose [34]. In the following, we refer to it as NP extraction. According to the peeling theorem [87,88], a certain component of the conformal Weyl tensor obeys the slowest $1/r$ falloff from the source, and hence is identified as outgoing gravitational radiation:

$$C_{\alpha\beta\gamma\delta} = \frac{\Psi_4}{r} + \frac{\Psi_3}{r^2} + \frac{\Psi_2}{r^3} + \frac{\Psi_1}{r^4} + \frac{\Psi_0}{r^5} + \mathcal{O}(r^{-6}). \tag{51}$$

Here, the slowest falloff is obeyed by the NP scalar Ψ_4, which is defined as[1]

$$\Psi_4 \equiv -C_{\alpha\beta\gamma\delta} n^\alpha \bar{m}^\beta n^\gamma \bar{m}^\delta, \tag{52}$$

where $C_{\alpha\beta\gamma\delta}$ is the conformal Weyl tensor associated with the 4-metric $g_{\alpha\beta}$ and $n, \bar{m}$ are part of a null tetrad [34,35] ℓ, n, m, $\bar{m}$ which satisfies $-\ell\cdot n = 1 = m\cdot\bar{m}$ while all other inner products vanish. In addition, this tetrad is related to the 4-metric via $g_{ab} = l_a n_b + l_b n_a - m_a\bar{m}_b - m_b\bar{m}_a$. At future null infinity $\mathcal{J}^+$, the topology of the spacetime is a time succession of spheres, $S^2\times\mathbb{R}$. Hence the simplest choice for the null tetrad at $\mathcal{J}^+$ is such that it resembles the unit sphere metric. Moreover, the simplest choice for a coordinate system at $\mathcal{J}^+$ is given by the Bondi gauge [87,88], which makes use of an areal radius coordinate.

In most current numerical relativity simulations, the radiation is computed at a *finite* radius, where the Bondi coordinates are usually not imposed. Rather, we use the gauge as evolved by the 1 + log slicing and Γ-driver conditions discussed in Sec. II B. In practice, we impose a simple polar-spherical coordinate system with constant coordinate radius $R^2 = x^2 + y^2 + z^2$, which does not take into account the background geometry, and hence does not make use of an areal radius. Thus, the gravitational radiation as computed on these coordinate spheres is not measured in the correct gauge, and leads to a systematic error that needs to be assessed. Note that it is principally possible to transform to the correct gauge [90].

In our construction of an approximate tetrad, we follow common practice (e.g. [91–93]) and use a triad of spatial vectors u, v, w obtained via a Gram-Schmidt orthonormalization starting from

$$u^i = [x, y, z], \tag{53}$$

$$v^i = [xz, yz, -x^2 - y^2], \tag{54}$$

$$w^i = \epsilon^i{}_{mn} v^m w^n, \tag{55}$$

where x, y, z are Cartesian coordinates of the computational grid and ϵ^{imn} is the three-dimensional Levi-Civita symbol. The tetrad is given in terms of this triad and the timelike normal vector $\hat{n}^\alpha$ by

$$\ell^\alpha = \frac{1}{\sqrt{2}}(\hat{n}^\alpha + u^\alpha), \tag{56}$$

$$n^\alpha = \frac{1}{\sqrt{2}}(\hat{n}^\alpha - u^\alpha), \tag{57}$$

$$m^\alpha = \frac{1}{\sqrt{2}}(v^\alpha + iw^\alpha). \tag{58}$$

A straightforward calculation shows that we are thus able to express Ψ_4 exclusively in terms of the "3 + 1" variables according to

$$\Psi_4 = \frac{1}{2}[E_{mn}(w^m w^n - v^m v^n) + B_{mn}(v^m w^n + w^m v^n)] + \frac{i}{2}[E_{mn}(v^m w^n - w^m v^n) + B_{mn}(w^m w^n + v^m v^n)], \tag{59}$$

where the electric and magnetic parts of the Weyl tensor are defined as [94]

$$E_{\alpha\beta} \equiv \perp^\mu_\alpha \perp^\nu_\beta C_{\mu\rho\nu\sigma}\hat{n}^\rho\hat{n}^\sigma, \tag{60}$$

[1]Our definition proceeds along the lines of Appendix C of Ref. [89], but for comparison with the quadrupole results, we define the Newman-Penrose scalar with the opposite sign of their Eq. (C1).

$$B_{\alpha\beta} \equiv \perp^{\mu}_{\alpha} \perp^{\nu *}_{\beta} C_{\mu\rho\nu\sigma}. \tag{61}$$

Here the $*$ denotes the Hodge dual and $\perp^{\mu}_{\alpha} \equiv \delta^{\mu}_{\alpha} + \hat{n}^{\mu}\hat{n}_{\alpha}$ is the projection operator. The Gauss-Codazzi equations (see e.g. [95]) enable us to calculate the electric and magnetic parts from the $3+1$ variables according to

$$E_{ij} = R_{ij} - \gamma^{mn}(K_{ij}K_{mn} - K_{im}K_{jn}), \tag{62}$$

$$B_{ij} = \gamma_{ik}\epsilon^{kmn}D_m K_{nj}. \tag{63}$$

In a given numerical simulation, we calculate Ψ_4 from Eq. (59) on a set of coordinate spheres defined by $R_{\rm ex} = \text{const}$. On each of these spheres, we use spin-weighted spherical harmonics ${}_{-2}Y_{\ell m}(\theta, \phi)$ of spin weight -2 in order to decompose the resulting wave signal into multipoles,

$$\begin{aligned} \Psi_4(t, \theta, \phi) &= \sum_{\ell,m} \Psi_4^{\ell m}(t)\, {}_{-2}Y_{\ell m}(\theta, \phi), \\ \Psi_4^{\ell m}(t) &= \int \Psi_4(t, \theta, \phi)\, {}_{-2}\bar{Y}_{\ell m}(\theta, \phi) d\Omega. \end{aligned} \tag{64}$$

In all our simulations, the wave signal is dominated by the $\ell = 2, m = 0$ mode whose angular dependence is given by

$${}_{-2}Y_{20} = \sqrt{\frac{15}{32\pi}} \sin^2\theta. \tag{65}$$

The NP scalar Ψ_4 is related to the gravitational wave strain via

$$\Psi_4 = \ddot{h}_+ - i\ddot{h}_\times. \tag{66}$$

It is convenient to decompose the two GW polarizations into multipoles in analogy to Eq. (64),

$$h_+ - ih_\times = \sum_{\ell=2}^{\infty} \sum_{m=-\ell}^{\ell} [h_+^{(\ell m)}(t) - ih_\times^{(\ell m)}(t)]\, {}_{-2}Y_{\ell m}(\theta, \phi). \tag{67}$$

These multipoles are related to those of the NP scalar by

$$\Psi_4^{\ell m} = \ddot{h}_+^{(\ell m)} - i\ddot{h}_\times^{(\ell m)}. \tag{68}$$

Note that the final result is not fully gauge invariant and contains an unknown amount of systematic error. The reasons are twofold: First, we did not choose a proper Bondi null tetrad on our extraction spheres, and, second, the extraction spheres have finite radius, and thus are neglecting nonlinear backscattering effects of the gravitational field in the wave zone. However, since our coordinate frame asymptotically approaches the Minkowski spacetime, both errors can be minimized by performing extrapolation to future null infinity $\mathcal{J}^+$, using a set of extraction spheres at finite radii. Unfortunately, even if the extrapolation is accurate, an uncertain amount of residual error may remain. In Sec. IV C, we check how well the extracted waves approximate their asymptotic shape and magnitude.

D. Cauchy-characteristic extraction

To circumvent the problem of finite-radius extraction and to eliminate this systematic error, we apply the technique of CCE [45,47–49,96,97] to obtain the NP scalar Ψ_4 as discussed in the previous section,[2] in this case directly evaluated at future null infinity $\mathcal{J}^+$. The CCE technique couples an exterior characteristic evolution of the full Einstein equations to the interior strong-field $3+1$ Cauchy evolution of the spacetime.

Characteristic evolutions are based on null-hypersurface foliations of spacetime and have the advantage of allowing for a compactification of the radial coordinate component, thus allowing us to include future null infinity $\mathcal{J}^+$ on the computational grid [45]. Unfortunately, the characteristic formulation gives rise to the formation of caustics; i.e., the null rays on which the coordinate system is based can intersect in strong-field regions, leading to coordinate singularities. The scheme is therefore not well suited for the evolution of the actual GW source. Characteristic evolutions, on the other hand, are well adapted to the far-field region of spacetime and can efficiently evolve the metric fields out to $\mathcal{J}^+$, where it is possible to obtain Ψ_4 (and, hence, h) in a mathematically unambiguous and gauge-invariant way [46,97–99].

We therefore proceed as follows: We evolve the interior region containing the collapsing matter with the standard Cauchy formulation as described in Secs. II B and II C. During the Cauchy evolution, we store the 3-metric components, including lapse and shift, on coordinate spheres with fixed radius R_Γ defining the world tube Γ.

This world tube forms the inner boundary for the subsequent characteristic evolution of the Einstein equations. The full 4-metric can be reconstructed from the stored 3-metric components, the lapse and the shift at the inner boundary. Upon construction of proper initial data on an initial null hypersurface, which here we simply assume to be conformally flat, we have then fully specified any data necessary to evolve the fields out to $\mathcal{J}^+$. More details on the exact mathematical procedure can be found in [45,96]. The characteristic field equations are solved numerically using the PITT null evolution code [46]. The numerical implementation of CCE including results from binary black hole mergers is discussed in [47–49]. For the characteristic computational grid, we use $N_r = 397$ points in the radial direction and $N_{\rm ang} = 73$ points in each angular direction for the two stereographic patches covering the sphere. The characteristic time-step size equals that of the Cauchy evolution.

[2] Alternatively during this procedure, we also compute the Bondi news function [34] $\mathcal{N}$, which is related to the GW strain by only one integration in time. We find that the news function is less robust when residual matter is present at the world-tube location and therefore restrict our attention to Ψ_4 only.

After each characteristic time step, the NP scalar Ψ_4 is evaluated directly from the metric at $\mathcal{J}^+$ and transformed to the desired Bondi gauge [98]. Thus, the CCE method is free of gauge and near-zone effects and represents the most rigorous extraction technique. However, there is still some remaining systematic error that is due to the presence of matter at the world-tube locations. Since the current set of characteristic equations does not take into account any form of matter contribution, a nonzero stress-energy tensor introduces an unknown error. We therefore have to perform checks of the dependence of the waveforms on the world-tube locations. In principle, it is possible to also incorporate matter on the characteristic side [100], which we leave to future work.

We note that CCE does not remove the artificial outer grid boundary from the Cauchy evolution. Thus, inconsistencies arising from this boundary can, in principle, still influence the interior domain. It is possible to circumvent this problem by enlarging the computational domain so that the outer boundary is causally disconnected from the world-tube locations (see, e.g., [91] in the context of binary black holes). In simulations of core collapse, however, this is currently not computationally feasible, but experiments with varied outer boundary locations have shown that boundary effects are negligible for our current choice of boundary location.

Finally, we point out that inconsistencies in the characteristic and Cauchy initial data may lead to a loss of some nonlinear effects, even though we expect these problems to be very small (see [48]). These and the outer boundary issues highlighted above can be fully accounted for only by employing Cauchy-characteristic matching (e.g. [45]). This technique uses the characteristic evolution as a generator for Cauchy boundary data at the world tube; i.e. the world tube becomes a two-way boundary between Cauchy and characteristic evolution. In practice, Cauchy-characteristic matching has not yet been successfully implemented.

E. Remarks on integration and physical units

The NP scalar $\Psi_4^{\ell m}$ must be integrated twice in time to yield the strain h, which introduces an artificial ''memory'' [101], i.e., a nonlinear drift of the signal so that the wave train deviates from an oscillation about zero. This behavior cannot be explained by the two unknown integration constants, resulting, at most, in a linear drift.

As suggested in [102], this nonlinear drift is a consequence of random-walk-like behavior induced by numerical noise. In the present work, we make use of methods that are strictly valid only in pure vacuum, and at our extraction spheres the average matter densities are nonzero (see Table III). This systematic error can lead to an additional artificial low-frequency drift. In order to eliminate this effect, we use fixed-frequency integration (FFI) as proposed in [102]. The NP variable $\Psi_4^{20}(t)$ is Fourier transformed; the resulting spectrum is divided by f_0^2 for frequencies $f < f_0$ and divided by f^2 otherwise. An inverse Fourier transform then yields the strain $h_{\ell m}$ essentially free of spurious drifts and oscillations, given a proper choice of f_0.

Finally, we need to address the question of units. The gravitational wave strain $h_+ - ih_\times$ is, by construction, dimensionless. For comparison of waveforms at different extraction radii, it is convenient to compensate for the $1/D$ falloff of the strain, where D is the distance from the observer to the source, and to work with $Dh_+^{(\ell m)}$ and $Dh_\times^{(\ell m)}$ instead. In most of the following, we convert from code units, which are in $c = G = M_\odot = 1$, to cgs units when stating and plotting numerical results. The conversion factors we use are $1M_\odot = 1.4772 \times 10^5$ cm for length, and $1M_\odot = 0.004\,927$ ms for time. For simplicity, we state the radii of GW extraction spheres and world-tube radii in code units. These and their corresponding cgs values are listed in Table III.

IV. RESULTS

In this section, we compare the most reliable extraction method that contains the least amount of systematic errors, CCE, with the various other curvature-based extraction methods, i.e., RWZM and NP extraction (both at finite radii). We also perform a comparison with the quadrupole approximation which has been employed in virtually all core collapse simulations to date.

This section is structured as follows. First, we review briefly the morphology of the gravitational waveforms expected from rotating core collapse and bounce.

Second, we elaborate, in more detail, on the method with which we obtain the gravitational strain h from the quantities measured during the simulation. This is important, since the derived strain typically contains severe nonlinear drifts, making a proper analysis largely impossible without significant preprocessing.

Third, we assess the accuracy of each individual method; i.e., we analyze the radial dependence of the NP and RWZM extraction methods, since they are strictly valid only in an asymptotic frame at an infinite distance from the source, where any contributions from the stress-energy tensor vanish. Since the matter densities are nonzero at the CCE world-tube locations, we also analyze the radial dependence of the waveforms extracted via CCE.

Fourth, we compare the results obtained via NP and RWZM extraction, and the approximate QF with results obtained via CCE.

Finally, we perform a convergence check on the computed waveforms by using a set of three different resolutions.

A. Morphology of rotating core collapse waveforms

The core collapse models considered in this work remain nearly axisymmetric during collapse and emit

GWs predominantly via the even-parity $(\ell, m) = (2, 0)$ spherical harmonic mode. This mode has a maximum on the equator and, hence, we plot all waveforms as seen by an observer in the equatorial plane. We write $h_{+,e} \equiv h^{20}_{+\,-2}Y_{20}(\theta = \pi/2, \phi)$, where $_{-2}Y_{20}$ is the spin-weighted spherical harmonic with spin $s = -2$. Note that the $(\ell, m) = (2, 0)$ mode is axisymmetric, and thus, the equatorial strain $h_{+,e}$ has no ϕ dependence.

We convert to cgs units by using the transformation as discussed in Sec. III E, and we align the maxima of the waveforms such that they occur at $t = 0.0$ ms, corresponding roughly to the time of core bounce in each model.

The waveforms of the three models are shown in Figs. 1 (model A1B3G3), 2 (model A1B3G5), and 3 (model A3B3G3). All models exhibit a very similar behavior. Prior to core bounce ($t < 0$ ms), the matter undergoes an aspherical accelerated collapse. Because of this aspherical acceleration, the GW signal is monotonically rising until it peaks when the contracting inner core is drastically decelerated. This deceleration is caused by the sudden stiffening of the EOS as a result of nuclear repulsive forces which emerge when nuclear densities are reached. During this deceleration, the GW signal becomes rapidly negative, reaching its second peak (the "bounce peak") roughly when the core rebounds. Subsequently, the inner core undergoes a relaxation phase (ring-down) in which it loses its remaining pulsation energy by launching secondary shocks. This results in an oscillatory GW signal that decreases in amplitude as the core approaches its final equilibrium.

While the overall morphology of the GWs emitted by the three models is the same, there are subtle differences that are worth commenting on. Models A1B3G3 and A3B3G3 produce so-called type I signals [50] with a single pronounced major peak at core bounce. Since model A3B3G3 is more rapidly spinning, its inner core is more deformed, and hence produces a stronger GW signal at core bounce than model A1B3G3. Model A1B3G5 has a very small inner core at bounce and produces a type III signal that is characterized by a much less pronounced bounce peak and generally low-amplitude GW emission. Note that type II signals, characterized by *multiple* wide and pronounced bounce peaks seen in early work [50,103–106], have been demonstrated to disappear in simulations using general relativity and a proper electron-capture treatment [4,5].

B. Computing the strain

We first consider the computation of the strain $h_{+,e}$ from the RWZM formalism. Since our models emit GWs predominantly in the $(\ell, m) = (2, 0)$ even mode Q^+,

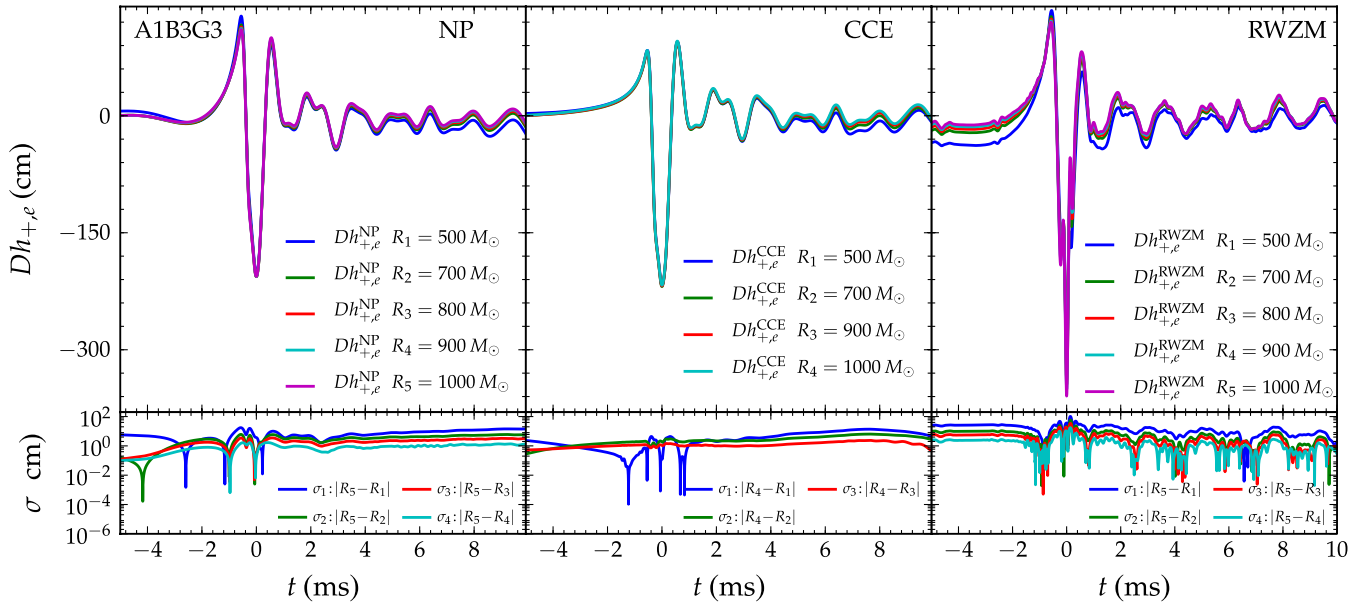

FIG. 1 (color online). Top panel (from left to right): $Dh^{NP}_{+,e}$ computed using NP extraction at radii $R_{ex} = (500, 700, 800, 900, 1000)M_\odot$, $Dh^{CCE}_{+,e}$ computed with CCE at $\mathcal{J}^+$ using world-tube data at $R_\Gamma = (500, 700, 900, 1000)M_\odot$, and $Dh^{RWZM}_{+,e}$ computed using the RWZM formalism at radii $R_{ex} = (500, 700, 800, 900, 1000)M_\odot$, all for model A1B3G3. Bottom panels: Absolute difference σ of the waves extracted at the various extraction radii and world-tube locations from those extracted at the outermost radius/location. The waveforms converge with increasing extraction radius and world-tube location. For NP extraction, we measure at the outermost detector sphere $R_{ex} = 1000M_\odot$ a maximum difference to the next closest detector $R_{ex} = 900M_\odot$ of $\sigma_4 = 2$ cm, which corresponds to a percentage error of $\sim$1% relative to the maximum. For CCE, we measure a maximum difference of $\sigma_4 = 1.5$ cm, corresponding to a percentage error of $\sim$0.7% relative to the maximum. For RWZM extraction, we have $\sigma_4 = 14$ cm, corresponding to $\sim$4% relative to the maximum. We note that RWZM is subject to additional high-frequency features and also contains a spurious spike in the bounce peak.

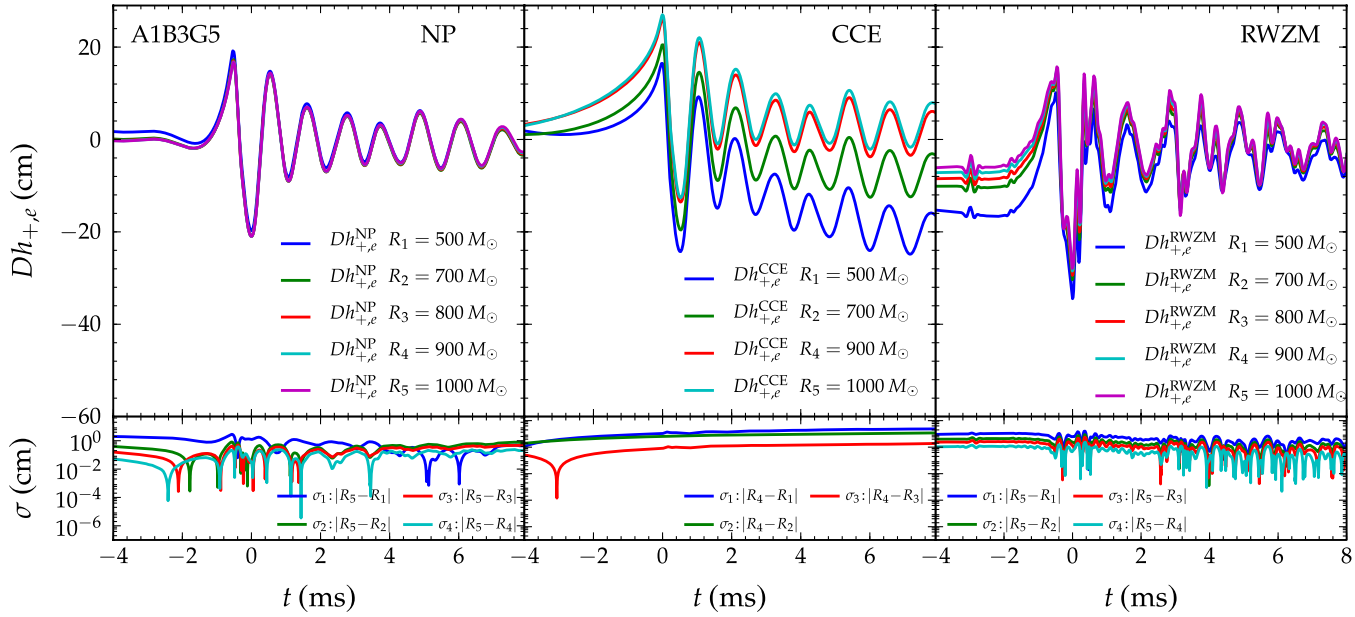

FIG. 2 (color online). Radial dependence of waveforms computed for model A1B3G5. See caption of Fig. 1 for details. For NP extraction, we measure at the outermost detector sphere $R_{\rm ex} = 1000M_\odot$ a maximum difference of $\sigma_4 = 0.4$ cm to the next closest detector $R_{\rm ex} = 900M_\odot$. This corresponds to a percentage error of $\sim$2% relative to the maximum. For CCE, we measure a maximum difference of $\sigma_4 = 1.6$ cm, corresponding to a percentage error of $\sim$6% relative to the maximum. For RWZM extraction, we have $\sigma_4 = 2.4$ cm, corresponding to $\sim$8% relative to the maximum. We note that RWZM is subject to strong additional high-frequency features. We also note that, while CCE shows for this model a larger error due to matter effects than finite-radius Ψ_4 extraction, it is more accurate at low frequencies (cf. Table II).

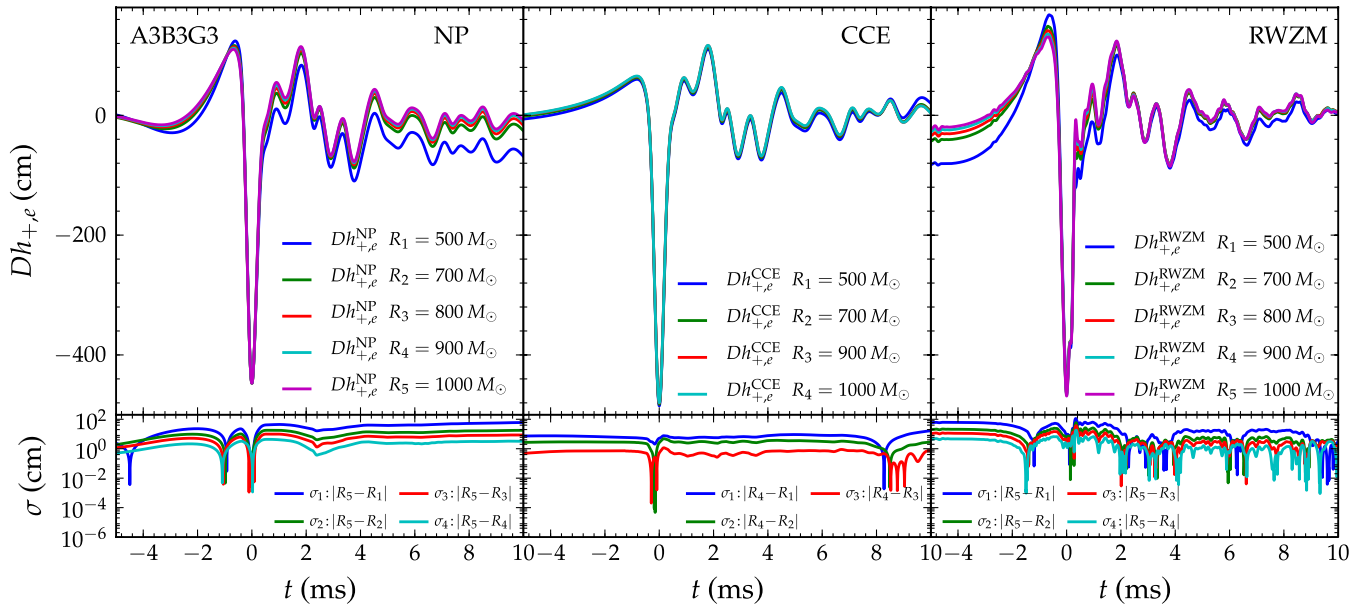

FIG. 3 (color online). Radial dependence of waveforms computed for model A3B3G3. See caption of Fig. 1 for details. For NP extraction, we measure at the outermost detector sphere $R_{\rm ex} = 1000M_\odot$ a maximum difference of $\sigma_4 = 2$ cm to the next closest detector $R_{\rm ex} = 900M_\odot$. This corresponds to a percentage error of $\sim$1% relative to the maximum. For CCE, we measure a maximum difference of $\sigma_4 = 1$ cm, corresponding to a percentage error of $\sim$0.2% relative to the maximum. For RWZM extraction, we have $\sigma_4 = 17$ cm, corresponding to $\sim$4% relative to the maximum.

the computation of the strain from the even- and odd-parity RWZM master functions reduces to Eq. (50) so that no time integral is necessary to obtain $h_{+,e}$. However, we still notice an unphysical drift in the waves. Since the RWZM master functions are computed at a *finite* distance from the source, we have the following systematic errors (summarized as the "finite-radius error"): (i) a nonvanishing matter density at the extraction spheres, (ii) near-zone effects, and (iii) gauge ambiguities. The latter error arises as a result of deviations from the Bondi gauge (see [90] for an improvement). The artificial drift is part of the finite-radius error, since it is becoming less pronounced with increasing extraction radius.

In order to reduce the contribution of these artificial low-frequency components, we first transform to the Fourier domain, multiply by f in order to take the first time derivative, and then apply fixed FFI [102] to obtain $h_{+,e}$. This procedure effectively acts as a filter that suppresses unwanted low-frequency components and at the same time minimizes spurious oscillations in the time domain such as Gibbs ringing or additional nonlinear low-frequency drifts.

The QF [cf. Eq. (36)] directly computes the strain and does not suffer from low-frequency drifts. However, the NP and CCE methods compute the second time derivative of the strain and, hence, must be integrated twice in time [Eq. (66)]. For this, we employ FFI to minimize the influence of artificial low-frequency components. Unfortunately, the time integration is still subject to some amount of low-frequency error, as we shall discuss in the following.

Error in the time integration

FFI introduces a free parameter f_0 that must be chosen based on the expected lowest *physical* frequency component of the signal. It must be larger than the spurious artificial low-frequency contributions that are introduced by aliased numerical noise and spectral leakage [102].

Unfortunately, in the case considered here, the artificial low-frequency contributions overlap with the low-frequency part of the physical signal. Since it is not possible to disentangle physical from artificial contributions at a given frequency, we have to choose an f_0 that is larger than the highest *unphysical* frequency contained in the signal. Thus, part of the overlapping *physical* low-frequency spectrum is lost when constructing the strain h.

We identify the highest unphysical frequency by choosing a set of different f_0 for a given waveform [i.e., we introduce a family of strains $h(t; f_0)$] and by imposing a relative maximum deviation $\max_t \delta h(t; f_0)/\delta f_0$ between the resulting strains $h(t; f_0)$ during ring-down that is not larger than some small ϵ. Since the ring-down phase is at the end of the wave train, the impact of the accumulated drift is largest here and can be clearly identified. Increasing f_0 reduces the drift in the ring-down phase, but also removes physical content, i.e., the monotonic rise of the signal in the prebounce phase. In order to gauge how much information is lost prior to core bounce, we compute the differences of $h(t; f_0)$ from the quadrupole waveform in an interval $t \in [-10\ \text{ms}, 0\ \text{ms}]$, since the quadrupole waveforms do not suffer from time integration issues and are presumably accurate up to at least the late prebounce phase. If we stop at some level of tolerance for any deviations $\max_t \delta h(t; f_0)/\delta f_0$ during ring-down and deviations from the quadrupole waveform prior to core bounce, we have identified an appropriate f_0. In practice, we choose a threshold $\max_t \delta D h(t; f_0)/\delta f_0 \lesssim \epsilon \sim 0.1$ cm/Hz during ring-down.

Our numerical experiments show that the cutoff frequency f_0 is model and extraction-method dependent and must be determined individually for any new set of initial data. In Table II, we list the frequencies f_0 for each of the considered models and extraction methods which yield the lowest deviations during ring-down and, at the same time, resemble as closely as possible the quadrupole waveform in the prebounce phase.

We find that NP and RWZM extraction, which both operate at finite radii, are subject to stronger drifts than the CCE method which computes the waveforms gauge invariantly at future null infinity $\mathcal{J}^+$. This is not surprising, given that the two former methods both suffer from near-zone and gauge errors which typically lead to low-frequency drifts in the waveform. Hence, the strain $h^{\text{CCE}}_{e,+}$ as computed by CCE retains most of the physical information at the low-frequency end of the spectrum, with a cutoff at $f_0 = 100$ Hz. Unfortunately, even this value may not be low enough, given that this frequency falls right into the band of highest sensitivity of km-scale ground-based detectors [107,108]. Not being able to resolve the low-frequency components is clearly a drawback of the curvature-based extraction methods.

Fortunately, as we will discuss in more detail in Sec. IV D 1, frequencies below 100 Hz do not contribute significantly to the inferred theoretical signal-to-noise ratio (SNR) for the models considered in this study or for the GW signal associated with core bounce in slowly to moderately rapidly rotating core collapse, in general [5]. Hence, at least the CCE method yields robust predictions for detection. A closer and more detailed comparison

TABLE II. Lowest possible physical frequencies that result in strain amplitudes with deviations $\max_t |\delta D h(t; f_0)/\delta f_0|$ of no more than $\epsilon \sim 0.1$ cm/Hz. In all cases, CCE yields the lowest possible f_0 and, hence, retains most physical information at the low-frequency end.

Method	A1B3G3 f_0 (Hz)	A1B3G5 f_0 (Hz)	A3B3G3 f_0 (Hz)
NP ($R_{\text{ex}} = 1000 M_\odot$)	300	300	250
RWZM ($R_{\text{ex}} = 1000 M_\odot$)	250	400	200
CCE ($R_\Gamma = 1000 M_\odot$)	100	100	100

between the waveforms computed with the various methods will be performed in Sec. IV D 1.

In the following, we use the cutoffs f_0 as given in Table II for the various models and extraction methods.

C. Radial dependence

The physical gravitational strain h scales $\propto 1/D$ with distance D, provided it is computed in an asymptotic frame at large distances from the source $D \to \infty$ (i.e., at astrophysical distances). At large asymptotic distances, we should therefore observe $Dh = \text{const}$. Since NP extraction and the RWZM formalism are evaluated at a finite distance from the source, they are both subject to finite-radius errors and we will generally not exactly observe $Dh = \text{const}$. Rather, we expect the signal to converge with increasing extraction radius towards its asymptotic shape and magnitude. In the context of vacuum binary black hole mergers, the asymptotic behavior and finite-radius error of NP extraction has been analyzed in Ref. [109], where it is found that extrapolations based on extractions at radii $R > 300M$, where M is the total mass of the system, yield acceptable results. In our case, however, the finite-radius error contains the additional error arising from nonzero matter content at the CCE world-tube locations and NP/RWZM extraction spheres.

In Table III, we summarize the time-averaged matter densities $\langle\rho\rangle$ at the various extraction spheres in our models. For simplicity, we do not compute the extraction-surface-averaged matter density but simply report the equatorial density at the various extraction spheres. The most compact model, A3B3G3, has $\langle\rho\rangle$ that are a factor of a few smaller at any given radius than in the other models. Therefore, we expect the systematic finite-radius error to be smallest in model A3B3G3.

In order to quantify the finite-radius error, we compute $Dh_{+,e}$ at a succession of extraction spheres with increasing radii $R_{\rm ex} = \{500M_\odot, 700M_\odot, 800M_\odot, 900M_\odot, 1000M_\odot\}$ and evaluate the differences. For $R_{\rm ex} \geq 1000M_\odot$, the spatial resolution of our computational grid becomes too coarse for accurate wave extraction and we limit our analysis to $R_{\rm ex} \leq 1000M_\odot$ (Table III). Note that for a given model and extraction method, we use the same cutoff frequency f_0 for all extraction radii and world-tube locations.

In principle, we should extrapolate the waveforms as obtained at the different extraction spheres to infinity. We observe, however, that the differences at large radii are within our numerical errors (see Sec. IV E) and asymptote rapidly. Therefore, we simplify the analysis by inspecting the behavior at successive radii without extrapolating. We will see in Sec. IV D 1 that this approach is justified. The CCE method, which does not require any extrapolation, shows good agreement with results obtained at finite radius within our numerical errors.

1. The NP scalar Ψ_4

In the upper left panels of Figs. 1–3, we show $Dh^{\rm NP}_{+,e}$ as computed from the NP scalar Ψ_4 for models A1B3G3, A1B3G5, and A3B3G3, respectively. In the bottom panel, we show the absolute differences σ between $Dh^{\rm NP}_{+,e}$ at $R_{\rm ex}$ from the reference distance at $R_{\rm ex} = 1000M_\odot$. In an ideal asymptotic frame, all curves would line up exactly. This is not the case in practice. We notice that the curves asymptote with increasing extraction radius; i.e., the differences σ between two successive extraction spheres converge to zero. This behavior shows that our extraction radii, albeit rather close to (and even inside) the star, lead to finite-radius errors for the waveforms computed from the NP scalar Ψ_4 that are below the discretization errors (cf. Sec. IV E). We measure a maximum absolute difference in amplitude of $\sigma \lesssim 2$ cm between the two outermost extraction spheres of any model (see lower panels of Figs. 1–3). This corresponds to a relative error of no more than $\sim 2\%$ when compared to the peak amplitudes.

Note that we had to cut off low frequencies (Table II) in order to remove spurious nonlinear drifts. This restricts our analysis to frequency components above the cutoff frequency f_0. Experiments show that for larger extraction radii, artificial low-frequency components become less prominent. Hence, extracting at greater radius would allow us to decrease f_0, but is presently too computationally demanding to be possible for production simulations.

TABLE III. Time-averaged equatorial matter densities and their variations at extraction radii for the computed models. The first two columns report the extraction radii in code units $M_\odot$ and in cgs units, respectively. All extraction surfaces are located on the fourth refinement level with a spatial resolution of $\Delta x = 8M_\odot$ ($\sim$11.82 km) and a time resolution of $\Delta t = 1.6M_\odot$ ($\sim 7.9 \times 10^{-6}$ s).

$R_{\rm ex}$ ($M_\odot$)	$R_{\rm ex}$ (km)	$\langle\rho\rangle$ A1B3G3 (g cm^{-3})	$\langle\rho\rangle$ A1B3G5 (g cm^{-3})	$\langle\rho\rangle$ A3B3G3 (g cm^{-3})
500	739	$(1.2 \pm 0.3) \times 10^8$	$(1.6 \pm 0.4) \times 10^8$	$(8.6 \pm 0.2) \times 10^8$
700	1034	$(2.3 \pm 0.4) \times 10^7$	$(2.6 \pm 0.5) \times 10^7$	$(1.3 \pm 0.3) \times 10^7$
800	1182	$(8.6 \pm 1.2) \times 10^6$	$(9.3 \pm 1.2) \times 10^6$	$(3.5 \pm 0.9) \times 10^6$
900	1329	$(3.0 \pm 0.4) \times 10^6$	$(3.3 \pm 0.4) \times 10^6$	$(5.5 \pm 1.6) \times 10^5$
1000	1477	$(9.3 \pm 0.6) \times 10^5$	$(1.2 \pm 0.6) \times 10^5$	$(2.5 \pm 2.2) \times 10^4$

2. The Regge-Wheeler-Zerilli-Moncrief formalism

The RWZM variables are computed as perturbations on an assumed fixed background spacetime. In an asymptotic frame at large distances from the source, they are independent of radius. As in the case for NP extraction, this is not achieved in practice, but the residual errors should converge with increasing extraction radius. We measure a relative difference in amplitude between the two outermost detector spheres of $\sigma \lesssim 17$ cm for all models (see the right panels of Figs. 1–3). This corresponds to a relative error of $\lesssim 8\%$ when compared to the maximum amplitudes and is significantly larger than what we find for NP extraction.

In addition, the RWZM method produces high-frequency variations in the waveform at core bounce and similar high-frequency features in the ring-down phase that are not seen in GWs extracted with the other methods. These features do not appear to converge with increasing radius; at least not at radii accessible to our simulations. They are particularly manifest in GWs of models producing weak signals, e.g., in the signal emitted by model A1B3G5 of our model set (Fig. 2). Furthermore, and most pronounced in model A1B3G3's waveform, a large spike during core bounce is visible in the RWZM result, but is not produced by any of the other methods (see Fig. 1 and the comparison in the upper panel of Fig. 4).

In order to investigate the cause of the differences seen with RWZM extraction, we perform a range of test calculations. These include (i) using two additional *independent* implementations of the RWZM method, one assuming a Minkowski background, the other using a generalization of the RWZM approach [110], (ii) performing a computationally very expensive simulation with extended grids, allowing for RWZM extraction at $R_{\rm ex} = 3000M_\odot$, (iii) performing simulations with up to a factor of 2 higher resolution and modified mesh refinement boundary locations, and (iv) changing the spacetime gauge conditions, including exponential damping of the evolution of the coordinate shift at large radii near the extraction spheres.

None of the above tests leads to any significant change of the RWZM result. This brings us to the conclusion that the high-frequency features observed in RWZM waveforms are systematic problems tied, most likely, to the particular perturbative nature of the RWZM scheme. One notable difference of the RWZM formalism from the other methods is the procedure of projecting out the spherical background geometry [e.g. Eq. (48)]. This can result in very small values for the aspherical perturbation coefficients that are prone to numerical noise and cancellation effects. The RWZM approach may therefore be less suitable for the extraction of the generally weak GW signals emitted in core collapse.

3. Radial dependence on world-tube location for CCE

The CCE method uses metric data from a time succession of finite-radius coordinate spheres, the world tube, as inner

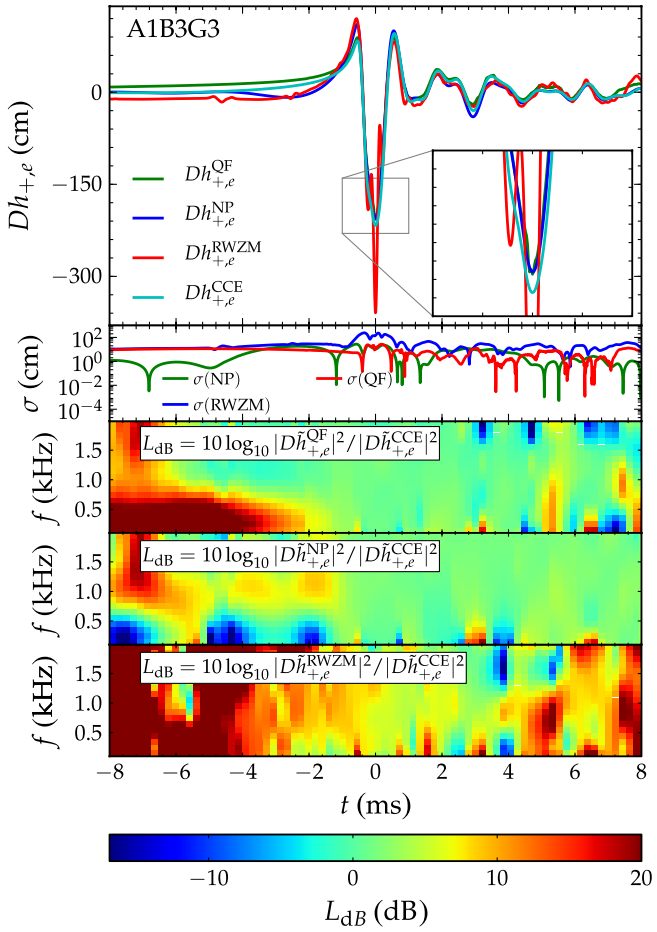

FIG. 4 (color online). Comparison of waveform amplitudes $Dh_{+,e}$, their absolute differences σ from CCE waveforms, and spectrograms of the power ratio $L_{\rm dB}$ between waveforms obtained from each extraction method and waveforms obtained via CCE for model A1B3G3. If $L_{\rm dB} = 0$, the waveform of the particular extraction method yields equal power per time and frequency bin with respect to that obtained with CCE. This is indicated by green colors. Blue colors indicate less power, and red colors indicate more power. See text for details. NP extraction and the quadrupole approximation yield remarkable agreement with CCE at frequencies below 2 kHz, at and after core bounce, while the RWZM formalism yields a spurious spike during core bounce and generally contains artificial high-frequency oscillations. This also becomes clear in the spectrograms of the power ratio between RWZM formalism and CCE since $L_{\rm dB} > 0$ over a wide range of time and frequencies (bottom panel). Prior to core bounce, -8 ms $< t < -1$ ms, NP extraction results in less power compared to CCE, while the QF yields more power.

boundary data for the evolution of the gravitational field out to $\mathcal{J}^+$. In vacuum, the method does not depend on the particular choice of any given world-tube radius [47,48]. However, the presence of matter at the world-tube location leads to a systematic error and imposes an artificial dependence of the waveforms computed at $\mathcal{J}^+$ on the world-tube

location. We plot in the center two panels of Figs. 1–3 the waveforms obtained at $\mathcal{J}^+$ using different world-tube radii as inner boundaries for the characteristic evolution. The center bottom panel of these figures depicts the absolute difference σ between the waveforms from the outermost world-tube radius at $R_\Gamma = 1000M_\odot$ and the waves from each of the smaller world-tube radii. It is apparent that the differences between the outermost two world-tube radii is always smallest, with absolute differences $\sigma < 1.6$ cm for all models and all times, and with an error relative to the maximum amplitude of $\lesssim 1\%$ for models A1B3G3 and A3B3G3, and $\sim 6\%$ for model A1B3G5. For the latter model, we also notice strong drifts at the innermost world-tube radii. Systematic errors due to the presence of matter can therefore become significant when the signal is weak and the density large. Note that the strong drift at the innermost world tubes may be removed by an increased FFI cutoff frequency of $f_0 = 150$ Hz in this case. Since we would like to retain as much physical information as possible, and since the outermost world-tube location permits $f_0 = 100$ Hz, we have chosen this value for all world tubes. Generally, the lower FFI cutoff frequency f_0 induces a more sensitive radial behavior with respect to low-frequency drifts. Since CCE permits a lower f_0 than NP extraction, the radial variations are slightly larger for CCE in model A1B3G5 when compared to the radial variations of NP extraction (cf. bottom panels of Fig. 2). In the other models, we find smaller radial variations between the two outermost CCE world tubes than between the two outermost NP extraction spheres (cf. bottom panels of Figs. 1 and 3), even though f_0 is smaller for CCE than for NP extraction in these models as well. This indicates that the remaining systematic nonzero matter error in CCE is not as important as the additional near-zone errors and gauge ambiguities inherent to NP extraction.

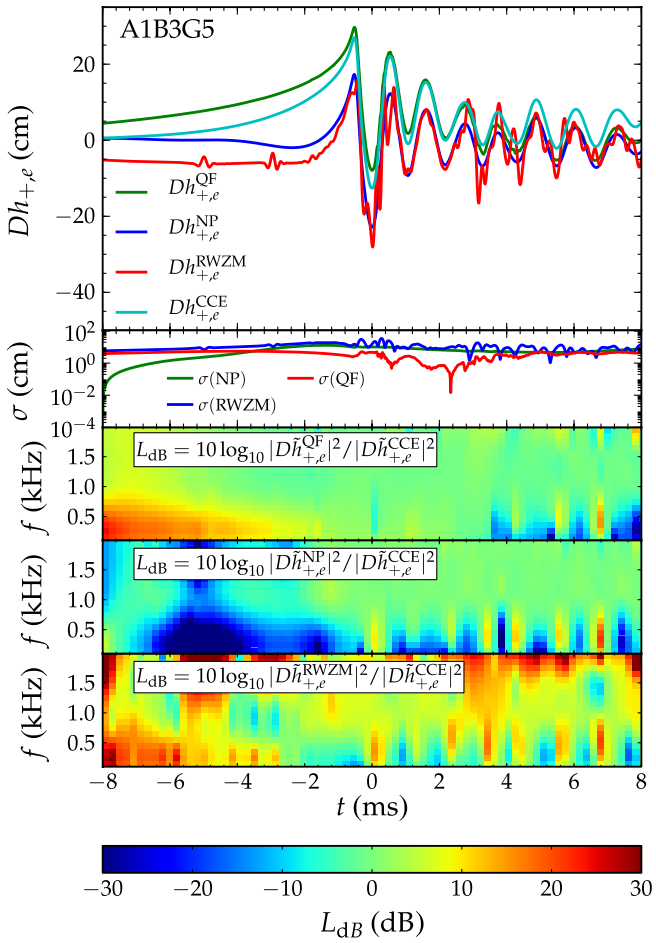

FIG. 5 (color online). Comparison of waveform amplitudes $Dh_{+,\varepsilon}$, their absolute differences σ to CCE waveforms, and spectrograms of the power ratio $L_{\rm dB}$ between waveforms obtained from each extraction method and waveforms obtained via CCE for model A1B3G5. If $L_{\rm dB} = 0$, the waveform of the particular extraction method yields equal power per time and frequency bin with respect to that obtained with CCE. This is indicated by green colors. Blue colors indicate less power, and red colors indicate more power. See text for details. The waveforms from NP extraction and quadrupole approximation agree well at frequencies below 2 kHz, at and after core bounce, while the RWZM formalism is subject to artificial high-frequency oscillations. The spectrograms of the power ratio between waveforms from the RWZM formalism and CCE in the bottom panel further support this, since $L_{\rm dB} > 0$ in this case. Prior to core bounce, -8 ms $< t < -1$ ms, NP extraction results in less power compared to CCE, while the QF yields more power.

D. Comparison

1. Comparison with Cauchy-characteristic extraction

CCE yields waveforms that contain the least amount of systematic errors compared to the other extraction methods considered in this work. It is completely gauge invariant and is free of near-zone errors. As found in Sec. , it is the only curvature-based method that captures most of the low-frequency band. Furthermore, as found in Sec. IV C, the remaining error due to the nonzero stress-energy tensor is small. We therefore use the waveforms obtained with CCE as a benchmark. In Figs. 4–6, we examine the waveforms as obtained by the various extraction methods, i.e., NP, RWZM, QF, and CCE for each model. In each figure, the top panel displays the amplitudes of the waves, $Dh_{+,\varepsilon}$, with the panel right below showing the absolute differences σ of each extraction method from CCE. It is apparent that in all cases the RWZM formalism yields the largest differences from CCE. As discussed in Sec. IV C, the RWZM formalism is subject to high-frequency noise and yields a large spurious spike at core bounce, most pronounced in model A1B3G3.

The quadrupole approximation and NP extraction only lead to small differences to CCE, in particular, at core bounce, but also in the ring-down part of the waveform. Moreover, it is surprising that the quadrupole formalism yields agreement so remarkably close to the results obtained via CCE, given the rather simplistic nature of the QF.

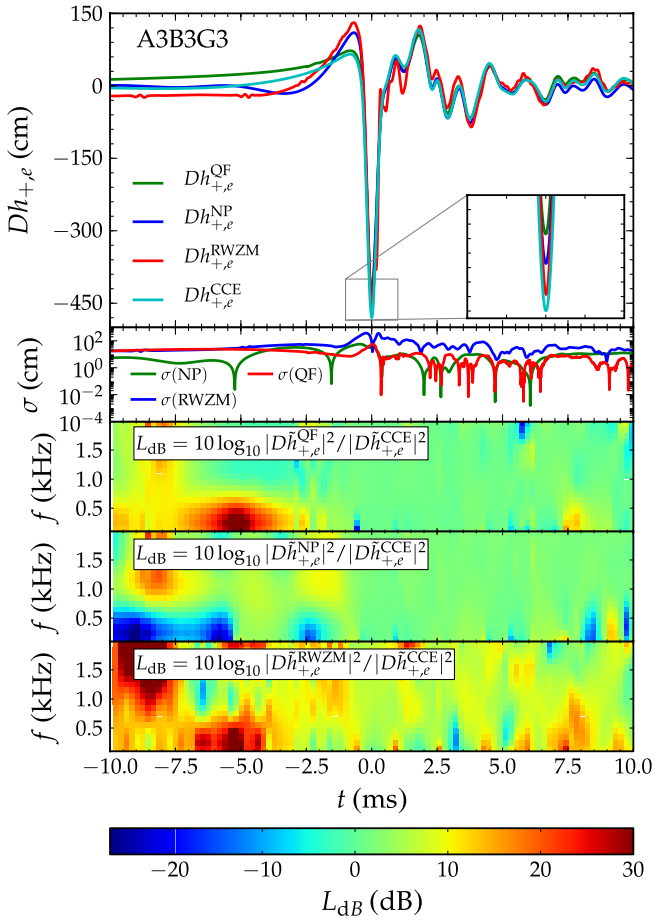

FIG. 6 (color online). Comparison of waveform amplitudes $Dh_{+,e}$, their absolute differences σ to CCE waveforms, and spectrograms of the power ratio $L_{\rm dB}$ between waveforms obtained from each extraction method and waveforms obtained via CCE for model A3B3G3. If $L_{\rm dB} = 0$, the waveform of the particular extraction method yields equal power per time and frequency bin with respect to that obtained with CCE. This is indicated by green colors. Blue colors indicate less power, and red colors indicate more power. See text for further explanation. The waveforms from NP extraction and from the quadrupole approximation agree well below 2 kHz, while the waveform from the RWZM formalism contains artificial high-frequency oscillations, thus leading to a higher power emission than waveforms obtained via CCE (bottom panel). Prior to core bounce, -10 ms $< t < -2$ ms, NP extraction results in less power compared to CCE, while the QF yields more power.

Quantitatively, when compared to the waveforms obtained via CCE, we find for model A1B3G3 that the waves obtained via the quadrupole approximation lead to smaller core-bounce peaks with differences up to $\sim$10 cm ($\sim$5%). For the same model, NP extraction results in core-bounce peaks that are smaller as well, with differences of $\sim$5%. Note, however, that in the NP waveform, the first positive peak prior to bounce is much larger, $\sim$31%, than what is predicted by CCE. The QF result, on the other hand, agrees much better with CCE at this peak ($\sim$5% overprediction).

For model A3B3G3, we find that at the bounce peak the QF (NP) amplitudes are $\sim$11% ($\sim$7%) smaller than the CCE prediction. For this model, the first positive peak before bounce is overpredicted by NP by $\sim$69%, while the QF yields an overprediction of only $\sim$11% compared to CCE.

A separate treatment is necessary for model A1B3G5. As briefly discussed in Sec. , the physical low-frequency components are filtered out by FFI in curvature-based extraction methods. The waveform of model A1B3G5 is most affected by this: Any physical low-frequency modulations or offsets are removed. Hence, the waveforms from curvature-based extraction are shifted downwards with respect to the QF waveform that does not require filtering. This shift leads to large absolute differences in the peak amplitudes by as much as ~ -10 cm at the first and second peaks when compared to the QF waveform, yielding relative differences by as much as $\sim$90% at core bounce. Constant (or nearly constant) offsets in the waveforms, however, are not visible to GW detectors. In order to get a better measure of the differences between the various extraction methods, we therefore compare the *change* in amplitude, $\delta Dh_{+,e} = |Dh^{t_1}_{+,e} - Dh^{t_2}_{+,e}|$, between the first and second peaks occurring at times t_1 and t_2, respectively. Compared to CCE, the change $\delta Dh^{\rm QF}_{+,e}$ measured in the quadrupole waves is $\sim$7% smaller, and $\delta Dh^{\rm NP}_{+,e}$ of the NP waveform is $\sim$1% larger.

Since a hypothetical matched-filtering GW search would be sensitive to differences in phase, an important aspect is the phase relation of the waveforms. A measure for the phase is given by the time lag between successive wave peaks, and we label the time of the peaks by $t_n = t_1, t_2, t_3, \ldots$ in their temporal order of occurrence. Note that in all cases, we have aligned the waveforms at the second peak occurring at $t_2 \equiv 0$ ms so that the time lag at this peak is zero for all methods and all models. We therefore measure the time lag $\delta t_{n,2}$ for a peak $t_{n\neq 2}$ relative to the second peak; e.g., we measure $\delta t_{1,2} = |t_2 - t_1|$. By comparing a number of time lags $\delta t_{n,2}$, we generally find that NP extraction, CCE, and QF produce the same phasing with an error of less than $\sim \pm 0.05$ ms for all peaks and all models. The differences in the time lags between successive wave peaks computed from the various extraction methods are therefore close to our time resolution of $\Delta t \approx 8 \times 10^{-3}$ ms. Note that the RWZM formalism is excluded from this analysis, since the additional high-frequency components make it hard to clearly identify the times of the maxima. Visual inspection suggests a phase error for RWZM comparable to the other methods, provided high-frequency contributions are ignored.

In the bottom three panels of Figs. 4–6, we plot spectrograms[3] of the power ratios $L_{\rm dB} = 10\log_{10}(P_1/P_0)$. Here,

[3]The spectrograms are made up of 100 time bins of 0.2 ms each and use a Hann window with a width of 2 ms.

the power spectrum $P_1 = |\tilde{h}(f)|^2$ is computed from the quadrupole approximation, NP extraction, and the RWZM formalism, respectively. The power spectrum $P_0 = |\tilde{h}_{\rm CCE}(f)|^2$ is computed from the waves obtained via CCE. At a given time t, the power spectra $P_{0,1}$ are obtained from the short-time Fourier transform of the strain over a time window of 2 ms centered at t. Thus, $L_{\rm dB}$ measures the power ratio per time and frequency bin of all extraction methods relative to the CCE method. If $L_{\rm dB} = 0$, the extraction method emits equal power per time and frequency bin and, hence, is equivalent to the waves from CCE. This is indicated by green (light gray) colors. Red (dark gray) regions indicate that waves obtained with the corresponding extraction method emit more power than the CCE waves during that time and frequency bin; blue (dark gray) indicates less power.

By inspection of the spectrograms, it is apparent that, at core bounce, the NP method and also the quadrupole approximation predict waves carrying roughly equal powers with respect to the waveforms obtained via CCE in a time interval of $[-4$ ms, 4 ms] and over the entire frequency range. Furthermore, we observe that in the prebounce phase $[-10$ ms, 4 ms], the quadrupole waves emit more power in low frequencies than the CCE waves, and the NP extracted waveforms emit less power. This is largely an effect of the different cutoff frequencies introduced in the integration of the waves obtained from the curvature-based methods (Table II).

We also find from the spectrograms that the RWZM extraction always deviates strongest from all other methods, primarily because its GWs contain spurious additional high-frequency components (cf. bottom panels of Figs. 4–6). This is clearly visible in the spectrograms, which show additional red ''speckles'' of higher emitted power throughout the wave train and frequency band.

As opposed to the quadrupole approximation, all curvature-based extraction methods are filtered below a frequency f_0 (Sec.). It is crucial to know whether the missing low frequencies can spoil the detectability of the GWs. To gauge the influence of low frequencies on the theoretical signal strength in GW detectors, we compute the theoretical optimal SNR for the quadrupole waveform, once including low-frequency contributions and once artificially cutting them off. The SNR is given by [111]

$$\rho_S^2 = 4\,\mathrm{Re}\int_0^\infty df\,\frac{|\tilde{h}(f)|^2}{S_h(f)}, \tag{69}$$

where $\tilde{h}$ is the Fourier transform of the strain h as measured at a distance $D = 10$ kpc to the source, and S_h is the one-sided noise power spectral density for a given detector, i.e., the detector sensitivity function.

Table IV lists, for all models, the theoretical optimal SNRs of waves extracted with the quadrupole formalism for the LIGO [107,112] detector and for the zero-detuning high-power configuration of advanced LIGO [108]. By cutting off at $f_0 = 100$ Hz (''QF, $f_0 = 100$ Hz''), we observe no significant reduction in SNR for models A1B3G3 and A3B3G3 and, hence, no loss of detectable GW information in rotating core collapse for these models. Model A1B3G5's type III waveform, on the other hand, has low-frequency components of high relative strength. In this model, a cutoff at $f_0 = 100$ Hz already leads to a SNR reduction by $\sim$17% ($\sim$ 23%) in LIGO (advanced LIGO).

When using 100 Hz $<$ f$_0$ $<$ 300 Hz as a cutoff, we find a reduction in SNR as large as $\sim$10%–30% for all models. Comparing to the cutoff frequencies required for FFI (Table II), this indicates that the finite-radius curvature-based NP and RWZM methods suffer from their inability to properly resolve frequencies in the range 100 Hz $<$ f $<$ 300 Hz.

TABLE IV. SNR ρ_S according to Eq. (69) for all models and all extraction methods at a distance $D = 10$ kpc for LIGO (top) and advanced LIGO (bottom). Note that we take into account only those frequencies above a given f_0 that have been determined to be reliable (see Table II). Since the quadrupole formalism is robust at low frequencies, we can gauge the influence of the neglected frequencies by additionally computing the SNR for the quadrupole waveform with the same low-frequency cutoff. For LIGO, we find no loss in SNR. For advanced LIGO the loss is at $\sim$1%. An exception is model A1B3G5, where the low-frequency components contribute significantly to the total emission.

Method	A1B3G3 ρ_S	A1B3G5 ρ_S	A3B3G3 ρ_S
LIGO			
QF	3.5	0.6	7.8
QF ($f_0 = 100$ Hz)	3.5	0.5	7.8
NP ($R_{\rm ex} = 1000M_\odot$)	3.1	0.4	7.4
RWZM ($R_{\rm ex} = 1000M_\odot$)	6.9	0.7	17.0
CCE ($R_\Gamma = 1000M_\odot$)	3.8	0.5	8.5
Advanced LIGO			
QF	49	9	95
QF ($f_0 = 100$ Hz)	49	7	94
NP ($R_{\rm ex} = 1000M_\odot$)	49	6	96
RWZM ($R_{\rm ex} = 1000M_\odot$)	105	12	209
CCE ($R_\Gamma = 1000M_\odot$	52	7	103

As shown in Table IV, the theoretical optimal SNRs as computed from the waves obtained for models A1B3G3 and A3B3G3 via CCE are essentially unaffected by low-frequency removal. Instead, they yield a slightly increased SNR compared to the QF result. This is due mostly to the higher amplitudes of the CCE waves at core bounce. Since low-frequency components are missing, model A1B3G5 is subject to a loss in SNR. CCE yields SNRs for LIGO and advanced LIGO that are identical to those obtained with QF with a cutoff at $f_0 = 100$ Hz (''QF, $f_0 = 100$ Hz'').

The RWZM method always overpredicts the SNR by $\sim$40%–100%. The reason is apparent from the

spectrograms in the bottom panels of Figs. 4–6, in which spurious additional high-frequency components lead to artificially high GW power and a corresponding overestimate of the SNR.

The waves computed with NP extraction show a high degree of agreement in SNR with the waves obtained with the QF. This, however, is misleading, since there are two balancing effects: (i) NP extraction predicts a higher amplitude in the first peak prior to core bounce, which would yield a larger SNR, but (ii) in NP extraction we must cut off frequencies $f < 300$ Hz, which artificially reduces the SNR.

Finally, we address the question of whether the waves obtained with the various extraction methods are within the tolerance for detection in a (hypothetical) matched-filtering GW data analysis of LIGO and advanced LIGO. Ideally, waveforms for the same model lead to a detection of the same model parameters and hence should not be distinguishable within a given threshold.

The (dis)agreement of waveforms obtained from different methods can be quantified by the mismatch (see, e.g., [113,114])

$$\mathcal{M}_{\rm mis} = 1 - \mathcal{M}, \tag{70}$$

where the *best* match $\mathcal{M}$ is given by

$$\mathcal{M} = \max_{t_0} \max_{\phi_1} \max_{\phi_2} \mathcal{O}[h_1, h_2], \tag{71}$$

which involves a maximization over time of arrival t_0 and the two phases ϕ_1 and ϕ_2 of the two wave signals h_1 and h_2, respectively. The overlap $\mathcal{O}$ between two waveforms is given by

$$\mathcal{O}[h_1, h_2] := \frac{\langle h_1|h_2\rangle}{\sqrt{\langle h_1|h_1\rangle\langle h_2|h_2\rangle}}, \tag{72}$$

with the detector-noise weighted scalar product

$$\langle h_1|h_2\rangle = 4\,\mathrm{Re}\int_0^\infty df\,\frac{\tilde{h}_1(f)\tilde{h}_2^*(f)}{S_h(f)}. \tag{73}$$

A mismatch $\mathcal{M}_{\rm mis}$ of zero indicates that waveforms h_1 and h_2 are identical. Conversely, a mismatch of $\mathcal{M}_{\rm mis} = 1$ indicates that the waveforms are completely different. In Table V, we list the mismatches between each of the extraction methods and the CCE method for all models. Note that we compute the mismatch starting from $f_0 = \max\{f_0^{(1)}, f_0^{(2)}\}$, where $f_0^{(1)}$ and $f_0^{(2)}$ are the lower cutoff frequencies as listed in Table II for the waveforms h_1 and h_2, respectively, since we do not trust waveforms below their value of f_0. We find that in all cases, the quadrupole approximation agrees best with waveforms obtained via CCE with mismatches to within 1% or better: We find a mismatch in the quadrupole waveforms to CCE of 0.6% (0.4%) for LIGO (advanced LIGO) for model A1B3G3, 1.3% (0.7%) for LIGO (advanced LIGO) for model A1B3G5, and 0.2% (0.2%) for LIGO (advanced LIGO) for model A3B3G3. As reported in Table V, NP extraction leads to slightly larger mismatches, due mainly (i) to less emitted power in the low-frequency band at and above this method's cutoff frequency, and (ii) to higher emitted power in the first wave peak (cf. spectrograms in second-lower panels of Figs. 4–6). The RWZM formalism performs worst for models producing weak signals, e.g., model A1B3G3 and, in particular, model A1B3G5. This is due primarily to the artificial high-frequency components produced by this method. Note that the mismatch discussed above depends on the cutoff frequency f_0. As a result, the range of frequencies contributing to the mismatch calculation is greatest for CCE-QF and smallest for CCE-RWZM. Hence, a full unbiased one-to-one comparison of the computed mismatches is not possible.

TABLE V. Mismatch $\mathcal{M}_{\rm mis}$ according to Eq. (70) for all models between CCE and the other extraction methods for the LIGO (top) and advanced LIGO detector (bottom). Note that we take into account only those frequencies above a given f_0 that have been determined to be reliable (see Table II). The waveforms from the quadrupole approximation yield the smallest mismatch to the waves from CCE, except in model A1B3G3. But note that the quadrupole approximation yields waveforms that allow the inclusion of lower frequencies than all other methods and hence allow the computation of the mismatch over a greater frequency range (only limited by the cutoff frequency of CCE), which introduces a small bias.

Method	A1B3G3 $\mathcal{M}_{\rm mis}$	A1B3G5 $\mathcal{M}_{\rm mis}$	A3B3G3 $\mathcal{M}_{\rm mis}$
LIGO			
NP ($R_{\rm ex} = 1000M_\odot$)	5×10^{-3}	19×10^{-3}	8×10^{-3}
RWZM ($R_{\rm ex} = 1000M_\odot$)	12×10^{-3}	38×10^{-3}	5×10^{-3}
QF	6×10^{-3}	13×10^{-3}	2×10^{-3}
Advanced LIGO			
NP ($R_{\rm ex} = 1000M_\odot$)	3×10^{-3}	12×10^{-3}	7×10^{-3}
RWZM ($R_{\rm ex} = 1000M_\odot$)	14×10^{-3}	48×10^{-3}	7×10^{-3}
QF	4×10^{-3}	7×10^{-3}	2×10^{-3}

We next investigate the implications of the mismatch on detecting a particular model in a matched-filtering analysis. A reduction in the match $\mathcal{M}$ is equivalent to a reduction in strain amplitude of the exact signal h (which here we assume to be given by the waveform computed via CCE) by $\mathcal{M}h$, hence effectively reducing the range of a GW detector by a factor of $\mathcal{M}$. To zeroth-order approximation, the number of detected events is proportional to the range cubed. A reduction in range by $\mathcal{M}$ means a reduction of the number of detectable events by $\mathcal{M}^3$. If we require a loss of no more than 10% of all detectable events, the match (mismatch) between a template waveform and the exact signal must therefore never go below (above) $\mathcal{M} = 0.965$ ($\mathcal{M}_{\rm mis} = 3.5 \times 10^{-2}$) [113–115]. This indicates that when used as hypothetical templates in a matched-filtering analysis of the LIGO and advanced LIGO data stream, NP

extraction and the quadrupole approximation yield waveforms that are within the error tolerance, but RWZM is generally not.

Overall, we conclude that NP extraction performs slightly worse than the quadrupole approximation when compared to CCE. The main reasons for this are (i) that NP requires a higher low-frequency cutoff and is therefore missing important low-frequency components, (ii) that NP yields larger values for the first wave peak compared to what is obtained with CCE or the quadrupole approximation, and (iii) that the mismatches between NP and CCE waveforms are larger than those between the QF and CCE waveforms. The RWZM formalism is generally performing the worst since it produces artificial high-frequency contributions.

2. Variations of the quadrupole formula

In Figs. 7–9, we plot waveforms for models A1B3G3, A1B3G5, and A3B3G3, respectively, computed via the QF given in Eq. (36), its PV and VS variants (Sec. III A), and the waves as predicted by the CCE method. In the lower panel of these figures, we plot the absolute differences σ from the CCE method for each variant of the QF. At core bounce, the smallest difference from CCE for model A1B3G3 is predicted by the PV variant ($\sim 1\%$ overprediction), followed by the standard QF ($\sim 5\%$ underprediction), and finally the VS variant ($\sim 8\%$ underprediction). For model A3B3G3, we measure the smallest difference from CCE in the PV variant ($\sim 5\%$ underprediction), followed by the standard QF ($\sim 11\%$ underprediction), and the VS variant ($\sim 13\%$ underprediction). For model A1B3G5, the cutoff of low-frequency components leads to an offset of the CCE waveform compared to the waves obtained with the QF variants. We therefore compare the change in amplitude $\delta Dh_{+,e}$ between the first and second peaks. We find that when compared to CCE, the *change* $\delta Dh^{\rm PV}_{+,e}$ is $\sim 2\%$ smaller in the PV variant, $\sim 7\%$ smaller in the standard QF, and also $\sim 7\%$ smaller in the VS variant.

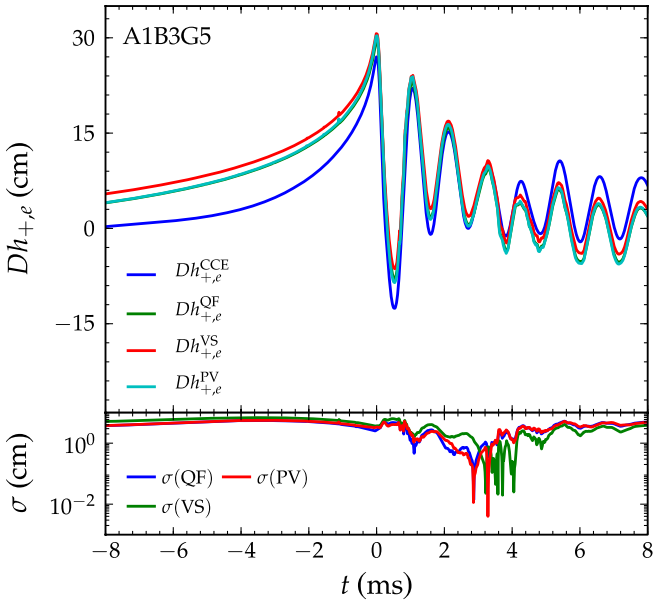

FIG. 8 (color online). Comparison of quadrupole to CCE waveforms for model A1B3G5. The PV variant results in the smallest differences of the *change* $\delta Dh_{+,e}$ between the first and second peaks (by $\sim 2\%$) compared to CCE.

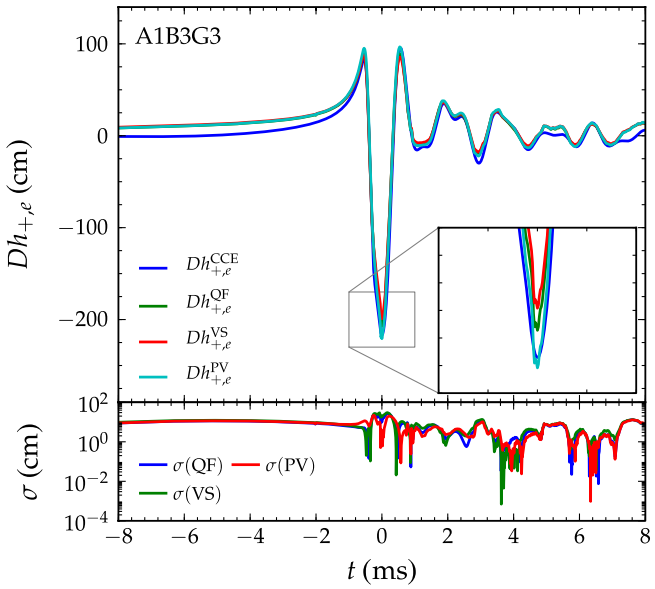

FIG. 7 (color online). Comparison of quadrupole to CCE waveforms for model A1B3G3. At and immediately after core bounce, the PV variant leads to a marginally smaller absolute difference from CCE ($\sim 1\%$) than any of the other QF variants.

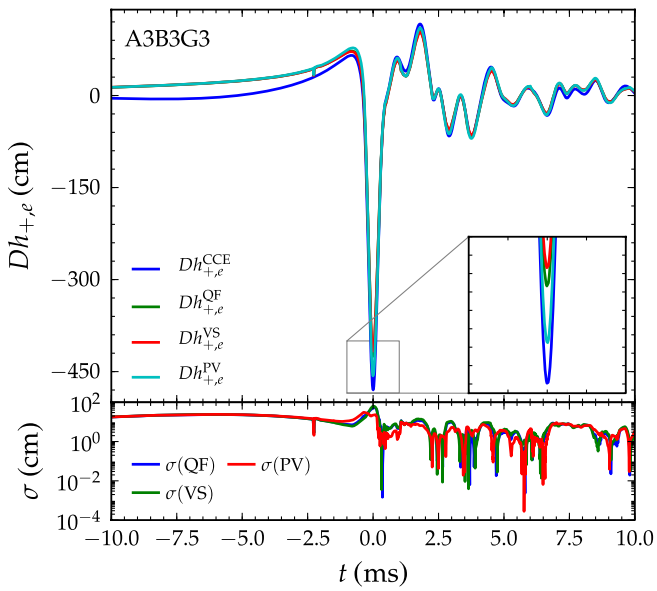

FIG. 9 (color online). Comparison of quadrupole to CCE waveforms for model A3B3G3. As for model A1B3G3 (Fig. 7), the PV variant leads to the smallest difference from CCE ($\sim 5\%$).

Overall, the waves computed with the PV variant are closest to the results obtained with the CCE method. Since the definition of the QF is ambiguous, this finding may depend on the particular system studied, and we cannot make strong general statements in support of one or the other variant.

E. Convergence

We check for convergence of our results via a resolution study of model A3B3G3 using three different resolutions, with finest resolutions $\Delta x = 0.3M_\odot$ (low), $\Delta x = 0.25M_\odot$ (medium; our baseline resolution), and $\Delta x = 0.20M_\odot$ (high).

In (relativistic) hydrodynamics simulations, convergence is notoriously difficult to analyze. The reasons are twofold: First, the occurrence of hydrodynamical shocks reduces the accuracy locally to first order. In our models, a shock appears right after core bounce and has significant impact on the order of convergence of our scheme. Second, our simulations are subject to some turbulence of the fluid motion appearing soon after bounce. Turbulence is stochastic in nature. Even a slight change of the resolution can result in completely different local behavior of the fluid. For this reason, it is impossible to check convergence locally at each grid point. Global quantities, however, should still be convergent. A sufficient global observable is the gravitational waveform, and we perform a convergence check on the waveform amplitudes.

Since we do not have an exact solution to compare with, we perform a three-level convergence check; i.e., we compute the ratio of the differences in the strain $Dh_{+,e}$ between the three resolutions,

$$C = \frac{|Dh^{\text{medium}}_{+,e} - Dh^{\text{low}}_{+,e}|}{|Dh^{\text{high}}_{+,e} - Dh^{\text{medium}}_{+,e}|}. \tag{74}$$

The ratio C defines the convergence *factor* of the solution, and can be translated into the order of convergence of the numerics, i.e., the convergence *rate*. Since our lowest order of accuracy is given by first-order near shocks, we expect at least first-order convergence.

Checking for convergence in the strain $Dh_{+,e}$ as computed from all extraction methods, we find a convergence factor of $C \gtrsim 1$ prior to core bounce and $C \sim 1$ after core bounce. For instance, in Fig. 10, we show a convergence plot of the waveform $Dh^{\text{CCE}}_{+,e}$ obtained from the CCE method.[4] In the upper panel, we show the waveforms obtained from three different resolutions, while in the lower panel, we show the differences between medium and low (blue curve) and high and medium resolutions (red curve). Given our resolutions, this convergence factor corresponds to a convergence rate between first and second orders prior to core bounce, which reduces to first order after core bounce.

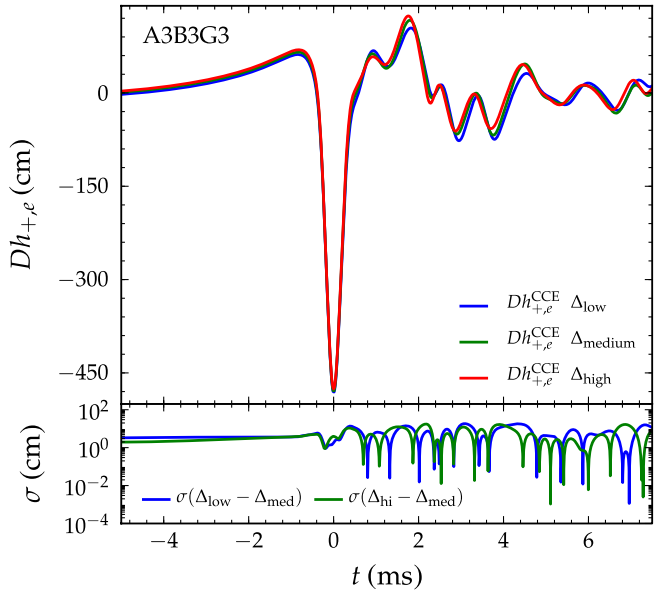

FIG. 10 (color online). Convergence of the waveform of model A3B3G3 as computed at $\mathcal{J}^+$ using CCE. In the bottom panel, we show the absolute differences σ between low and medium resolutions, and high and medium resolutions, respectively. Without rescaling any of the difference curves, we observe that they approximately line up at and after core bounce so that the convergence factor is simply given by $C \sim 1$. This indicates a convergence order at and after core bounce of 1. In the prebounce phase, the difference between medium and high resolutions is slightly smaller than the difference between medium and low resolutions, resulting in a slightly larger convergence factor. Given our resolutions, this factor corresponds roughly to second-order convergence.

We can estimate a numerical error in the medium resolution simulation by performing a Richardson extrapolation using the measured convergence rate on the computed waveform (see, e.g., [95]). This error estimate, however, can only be applied if the convergence rate is unambiguous. Since we measure a rate between first and second orders, this is not exactly the case here. Another measure of the numerical error in the medium resolution simulation is therefore directly given by the difference between medium- and high-resolution simulations. This is displayed by the green curve in the bottom panel of Fig. 10. At core bounce, we measure in the medium resolution simulation a relative numerical error of ~4%.

V. SUMMARY AND CONCLUSIONS

We have performed a comparison study of four currently available GW extraction techniques in the context of axisymmetric rotating stellar core collapse. This study is

[4]The characteristic computational grid resolutions are scaled by the same factors as the corresponding resolutions of the Cauchy evolution.

the first to succeed in extracting GWs directly from axisymmetric core collapse spacetimes and the first to employ the fully coordinate independent CCE extraction method for nonvacuum spacetimes.

We have performed core collapse simulations with simplified microphysics using a set of three representative initial configurations leading to GW signals of varying strength and signal morphology in quantitative agreement with what is expected from microphysically more complete models. In addition to having extracted waves with variants of the standard coordinate-dependent slow-motion, weak-field quadrupole formula, we have employed (i) the RWZM formalism, (ii) extraction based on the NP scalar Ψ_4, and (iii) CCE. Of these three latter curvature-based methods, RWZM and NP extract GWs at a finite radius from the source and, hence, are generally prone to systematic errors arising from (i) near-zone effects, (ii) gauge ambiguities, and (iii) nonvanishing matter contributions. The CCE method, on the other hand, extracts waves gauge invariantly at future null infinity $\mathcal{J}^+$, that is, at an infinite distance from the source where gravitational radiation is unambiguously defined. Hence, it is subject only to small systematic errors due to the presence of matter fields at the CCE world-tube locations.

An integral ingredient contributing to our success in extracting GWs from core collapse using curvature-based methods has been the removal of unphysical nonlinear low-frequency drifts from the waveforms that otherwise would make a proper analysis largely impossible. This has been achieved by the application of FFI [102] for time integration and filtering to yield the strain h.

Comparing the waveforms obtained with the various extraction methods, we make a number of observations: (i) NP- and CCE-extracted waveforms converge with extraction and world-tube radius, respectively. The waveforms obtained with the RWZM formalism show spurious high-frequency components that no other method reproduces. A number of tests imply that the RWZM method may be less applicable to weak GW signals, at least at the currently accessible numerical resolutions and grid sizes. (ii) NP extraction, CCE, and even the quadrupole approximation yield waveforms which agree well in phase, with differences in the time lags between successive peaks of $\lesssim 0.05$ ms. Since the RWZM formalism is contaminated by unphysical high-frequency components, an accurate determination of the phasing compared to the other methods is largely impossible. (iii) The maximum amplitudes at core bounce are different by $\sim$1%–7% in waveforms obtained with NP extraction and are systematically smaller by $\sim$5%–11% in waveforms obtained with the QF compared to the waves obtained via CCE. Accordingly, CCE yields waveforms that result in slightly higher SNRs ($\sim$6%–9%). (iv) Overall, the error of the waveforms computed with the quadrupole approximation are well within numerical errors and physical uncertainties. Unlike the waveforms obtained with the curvature-based methods, the quadrupole waveforms do not suffer from low-frequency drifts. In that respect, the quadrupole approximation is advantageous. We also observe that the quadrupole variant using ''physical'' velocity components [78] yields waves that are closer to those obtained via CCE. However, this finding may be true only for the core collapse case studied here and may not hold in general. (v) While it is unlikely that matched-filtering approaches will be used in searches for GWs from core collapse in the near future, we have nevertheless computed GW template mismatches, a measure for the detectability of differences between waveforms. We find that when used in hypothetical matched-filtering GW searches, waveforms from NP extraction, CCE, and the QF would lead to the detection of the same model, while the waveforms computed with the RWZM formalism generally would not.

There are two major drawbacks of our current work: (i) The curvature-based methods assume vacuum at the extraction spheres and world-tube locations. Hence, we must, in principle, extract at very large radii where the stress-energy tensor is zero. This, however, is currently not possible, since the collapsing star extends over the entire computational grid and larger grids are computationally prohibitive. (ii) All curvature-based methods yield waveforms with unphysical low-frequency drifts, requiring removal by spectral cutoff via FFI. This is particularly problematic in models with physical content below $\sim$100 Hz. A possible improvement of the low-frequency behavior could be achieved by the inclusion of matter terms in the CCE method or, alternatively, by enlarging the simulation domain such that the extraction takes place outside of the star and in pure vacuum. The latter could be efficiently achieved by employing multiblock techniques that cover the wave zone by a set of spherical grids [116].

Finally, we point out that we have considered only the GW signal from rotating core collapse and bounce in this first study using curvature-based GW extraction from core collapse spacetimes. While our results may transfer to other GW emission processes in core collapse, this is by no means guaranteed. Further work will be needed to address curvature-based GW extraction also from post-bounce convection and the standing accretion shock instability, protoneutron star pulsations, rotational instabilities, and black hole formation.

ACKNOWLEDGMENTS

We are happy to acknowledge helpful exchanges with E. Abdikamalov, P. Ajith, A. Burrows, N. T. Bishop, P. Cerdá-Durán, P. Diener, H. Dimmelmeier, J. Kaplan, E. O'Connor, E. Pazos, D. Pollney, E. Seidel, R. O'Shaughnessy, K. Thorne, and S. Teukolsky. This work is supported by the Sherman Fairchild Foundation and by the National Science Foundation under Grants No. AST-0855535, No. OCI-0721915, No. PHY-0904015,

No. OCI-0905046, and No. OCI-0941653. C. D. O. and C. R. wish to thank Chris Mach for support of the group servers at TAPIR on which much of the code development and testing was carried out. Results presented in this article were obtained through computations on the Caltech compute cluster "Zwicky" (NSF MRI Grant No. PHY-0960291), on the NSF Teragrid under Grant No. TG-PHY100033, on machines of the Louisiana Optical Network Initiative under Grant No. loni_numrel05, and at the National Energy Research Scientific Computing Center (NERSC), which is supported by the Office of Science of the U.S. Department of Energy under Contract No. DE-AC03-76SF00098. U. S. acknowledges support from the Ramón y Cajal Programme of the Spanish Ministry of Education and Science, from FCT-Portugal through Grant No. PTDC/FIS/098025/2008, and allocations through the TeraGrid Advanced Support Program under Grant No. PHY-090003 at NICS and the Centro de Supercomputación de Galicia (CESGA, Project No. ICTS-2009-40).

[1] H. A. Bethe, Rev. Mod. Phys. **62**, 801 (1990).
[2] E. Baron and J. Cooperstein, Astrophys. J. **353**, 597 (1990).
[3] C. D. Ott, Classical Quantum Gravity **26**, 063001 (2009).
[4] C. D. Ott, H. Dimmelmeier, A. Marek, H.-T. Janka, I. Hawke, B. Zink, and E. Schnetter, Phys. Rev. Lett. **98**, 261101 (2007).
[5] H. Dimmelmeier, C. D. Ott, A. Marek, and H.-T. Janka, Phys. Rev. D **78**, 064056 (2008).
[6] S. Scheidegger, S. C. Whitehouse, R. Käppeli, and M. Liebendörfer, Classical Quantum Gravity **27**, 114101 (2010).
[7] S. Scheidegger, R. Käppeli, S. C. Whitehouse, T. Fischer, and M. Liebendörfer, Astron. Astrophys. **514**, A51 (2010).
[8] T. Takiwaki and K. Kotake, arXiv:1004.2896 [Phys. Rev. D (to be published)].
[9] C. D. Ott, C. Reisswig, E. Schnetter, E. O'Connor, U. Sperhake, F. Loeffler, P. Diener, E. Abdikamalov, I. Hawke, and A. Burrows, arXiv:1012.1853.
[10] A. Burrows and J. Hayes, Phys. Rev. Lett. **76**, 352 (1996).
[11] C. L. Fryer, D. E. Holz, and S. A. Hughes, Astrophys. J. **609**, 288 (2004).
[12] C. D. Ott, A. Burrows, L. Dessart, and E. Livne, Phys. Rev. Lett. **96**, 201102 (2006).
[13] A. Marek and H.-T. Janka, Astrophys. J. **694**, 664 (2009).
[14] J. W. Murphy, C. D. Ott, and A. Burrows, Astrophys. J. **707**, 1173 (2009).
[15] K. Kotake, W. Iwakami, N. Ohnishi, and S. Yamada, Astrophys. J. Lett. **697**, L133 (2009).
[16] K. N. Yakunin *et al.*, Classical Quantum Gravity **27**, 194005 (2010).
[17] M. Shibata and Y.-I. Sekiguchi, Phys. Rev. D **71**, 024014 (2005).
[18] K. S. Thorne, in *300 Years of Gravitation*, edited by S. W. Hawking and W. Israel (Cambridge University Press, Cambridge, England, 1987).
[19] C. Röver, M. Bizouard, N. Christensen, H. Dimmelmeier, I. S. Heng, and R. Meyer, Phys. Rev. D **80**, 102004 (2009).
[20] T. Z. Summerscales, A. Burrows, L. S. Finn, and C. D. Ott, Astrophys. J. **678**, 1142 (2008).
[21] H. Dimmelmeier, J. A. Font, and E. Müller, Astron. Astrophys. **393**, 523 (2002).
[22] H. Dimmelmeier, J. Novak, J. A. Font, J. M. Ibáñez, and E. Müller, Phys. Rev. D **71**, 064023 (2005).
[23] M. Shibata and Y. Sekiguchi, Phys. Rev. D **69**, 084024 (2004).
[24] M. Shibata, Y. T. Liu, S. L. Shapiro, and B. C. Stephens, Phys. Rev. D **74**, 104026 (2006).
[25] C. D. Ott, H. Dimmelmeier, A. Marek, H.-T. Janka, B. Zink, I. Hawke, and E. Schnetter, Classical Quantum Gravity **24**, S139 (2007).
[26] T. Kuroda and H. Umeda, Astrophys. J. Suppl. Ser. **191**, 439 (2010).
[27] H. Dimmelmeier, C. D. Ott, H.-T. Janka, A. Marek, and E. Müller, Phys. Rev. Lett. **98**, 251101 (2007).
[28] M. Obergaulinger, M. A. Aloy, H. Dimmelmeier, and E. Müller, Astron. Astrophys. **457**, 209 (2006).
[29] K. S. Thorne, Rev. Mod. Phys. **52**, 299 (1980).
[30] T. Regge and J. A. Wheeler, Phys. Rev. **108**, 1063 (1957).
[31] F. J. Zerilli, Phys. Rev. Lett. **24**, 737 (1970).
[32] F. J. Zerilli, Phys. Rev. D **2**, 2141 (1970).
[33] V. Moncrief, Ann. Phys. (N.Y.) **88**, 323 (1974).
[34] E. T. Newman and R. Penrose, J. Math. Phys. (N.Y.) **3**, 566 (1962).
[35] R. Penrose, Phys. Rev. Lett. **10**, 66 (1963).
[36] M. Shibata and Y.-I. Sekiguchi, Phys. Rev. D **68**, 104020 (2003).
[37] L. Baiotti, S. Bernuzzi, G. Corvino, R. de Pietri, and A. Nagar, Phys. Rev. D **79**, 024002 (2009).
[38] A. Nagar, J. A. Font, O. Zanotti, and R. D. Pietri, Phys. Rev. D **72**, 024007 (2005).
[39] R. Oechslin, H.-T. Janka, and A. Marek, Astron. Astrophys. **467**, 395 (2007).
[40] C. Reisswig *et al.*, Phys. Rev. D **80**, 124026 (2009).
[41] C. O. Lousto, M. Campanelli, and Y. Zlochower, Classical Quantum Gravity **27**, 114006 (2010).
[42] C. D. Ott, Ph.D. thesis, Universität Potsdam, Potsdam, Germany, 2006 [http://nbn-resolving.de/urn/resolver.pl?urn=urn:nbn:de:kobv:517-opus-12986].
[43] P. Cerdá-Durán, G. Faye, H. Dimmelmeier, J. A. Font, J. M. Ibáñez, E. Müller, and G. Schäfer, Astron. Astrophys. **439**, 1033 (2005).
[44] F. Siebel, J. A. Font, E. Müller, and P. Papadopoulos, Phys. Rev. D **67**, 124018 (2003).

[45] J. Winicour, Living Rev. Relativity **8**, 10 (2005), http://www.livingreviews.org/lrr-2005-10.

[46] N. T. Bishop, R. Gómez, L. Lehner, M. Maharaj, and J. Winicour, Phys. Rev. D **56**, 6298 (1997).

[47] C. Reisswig, N. T. Bishop, D. Pollney, and B. Szilagyi, Phys. Rev. Lett. **103**, 221101 (2009).

[48] C. Reisswig, N. T. Bishop, D. Pollney, and B. Szilagyi, Classical Quantum Gravity **27**, 075014 (2010).

[49] M. C. Babiuc, B. Szilagyi, J. Winicour, and Y. Zlochower, arXiv:1011.4223.

[50] T. Zwerger and E. Müller, Astron. Astrophys. **320**, 209 (1997).

[51] E. B. Abdikamalov, C. D. Ott, L. Rezzolla, L. Dessart, H. Dimmelmeier, A. Marek, and H. Janka, Phys. Rev. D **81**, 044012 (2010).

[52] C. D. Ott, E. Schnetter, A. Burrows, E. Livne, E. O'Connor, and F. Löffler, J. Phys. Conf. Ser. **180**, 012022 (2009).

[53] T. Goodale, G. Allen, G. Lanfermann, J. Massó, T. Radke, E. Seidel, and J. Shalf, in *Vector and Parallel Processing—VECPAR'2002, 5th International Conference*, Lecture Notes in Computer Science (Springer, Berlin, 2003).

[54] CACTUS Computational Toolkit, http://www.cactuscode.org/.

[55] EINSTEIN TOOLKIT: A Community Toolkit for Numerical Relativity, http://www.einsteintoolkit.org.

[56] S. Scheidegger, T. Fischer, S. C. Whitehouse, and M. Liebendörfer, Astron. Astrophys. **490**, 231 (2008).

[57] J. W. York, in *Sources of Gravitational Radiation*, edited by L. L. Smarr (Cambridge University Press, Cambridge, England, 1979), pp. 83–126.

[58] E. Schnetter, Component-Based High Performance Computing, 2008.

[59] E. Schnetter, S. H. Hawley, and I. Hawke, Classical Quantum Gravity **21**, 1465 (2004).

[60] E. Schnetter, P. Diener, E. N. Dorband, and M. Tiglio, Classical Quantum Gravity **23**, S553 (2006).

[61] CARPET, Mesh Refinement with CARPET, http://www.carpetcode.org/.

[62] M. J. Berger and J. Oliger, J. Comput. Phys. **53**, 484 (1984).

[63] J. W. York, Jr., in *Sources of Gravitational Radiation*, edited by L. Smarr (Cambridge University Press, Cambridge, England, 1979), pp. 83–126.

[64] M. Alcubierre, B. Brügmann, T. Dramlitsch, J. A. Font, P. Papadopoulos, E. Seidel, N. Stergioulas, and R. Takahashi, Phys. Rev. D **62**, 044034 (2000).

[65] M. Alcubierre, B. Brügmann, P. Diener, M. Koppitz, D. Pollney, E. Seidel, and R. Takahashi, Phys. Rev. D **67**, 084023 (2003).

[66] D. Brown, P. Diener, O. Sarbach, E. Schnetter, and M. Tiglio, Phys. Rev. D **79**, 044023 (2009).

[67] D. Müller and B. Brügmann, Classical Quantum Gravity **27**, 114008 (2010).

[68] E. Schnetter, Classical Quantum Gravity **27**, 167001 (2010).

[69] MCLACHLAN, a Public BSSN Code, http://www.cct.lsu.edu/eschnett/McLachlan/.

[70] C. Lechner, D. Alic, and S. Husa, in SYNASC 2004—6th International Symposium on Symbolic and Numeric Algorithms for Scientific Computing, Timisoara, Romania (2004).

[71] S. Husa, I. Hinder, and C. Lechner, Comput. Phys. Commun. **174**, 983 (2006).

[72] KRANC: Automated Code Generation, http://numrel.aei.mpg.de/Research/Kranc/.

[73] L. Baiotti, I. Hawke, P. J. Montero, F. Löffler, L. Rezzolla, N. Stergioulas, J. A. Font, and E. Seidel, Phys. Rev. D **71**, 024035 (2005).

[74] J. W. York, Jr., in *Gravitational Radiation*, edited by T. Deruelle and N. Piran (North-Holland, Amsterdam, 1983), pp. 175–201.

[75] J. A. Font, Living Rev. Relativity **11**, 7 (2008).

[76] J. M. Hyman, *Tech. Rep., ERDA Mathematics and Computing Laboratory, Courant Institute of Mathematical Sciences* (New York University, New York, 1976).

[77] H.-T. Janka, T. Zwerger, and R. Mönchmeyer, Astron. Astrophys. **268**, 360 (1993).

[78] H. Dimmelmeier, J. A. Font, and E. Müller, Astron. Astrophys. **388**, 917 (2002).

[79] H. Komatsu, Y. Eriguchi, and I. Hachisu, Mon. Not. R. Astron. Soc. **237**, 355 (1989).

[80] H. Komatsu, Y. Eriguchi, and I. Hachisu, Mon. Not. R. Astron. Soc. **239**, 153 (1989).

[81] L. S. Finn and C. R. Evans, Astrophys. J. **351**, 588 (1990).

[82] L. Blanchet, T. Damour, and G. Schaefer, Mon. Not. R. Astron. Soc. **242**, 289 (1990).

[83] V. Moncrief, Ann. Phys. (N.Y.) **88**, 323 (1974).

[84] A. Nagar and L. Rezzolla, Classical Quantum Gravity **22**, R167 (2005).

[85] R. Arnowitt, S. Deser, and C. Misner, *Dynamics of General Relativity*, in Gravitation: An Introduction to Current Research (Wiley, New York, 1962).

[86] K. Camarda and E. Seidel, Phys. Rev. D **59**, 064019 (1999).

[87] H. Bondi, M. G. J. van der Burg, and A. W. K. Metzner, Proc. R. Soc. A **269**, 21 (1962).

[88] R. K. Sachs, Proc. R. Soc. A **270**, 103 (1962).

[89] U. Sperhake, Phys. Rev. D **76**, 104015 (2007).

[90] L. Lehner and O. M. Moreschi, Phys. Rev. D **76**, 124040 (2007).

[91] D. Pollney, C. Reisswig, E. Schnetter, N. Dorband, and P. Diener, arXiv:0910.3803 [Phys. Rev. D (to be published)].

[92] B. Bruegmann *et al.*, Phys. Rev. D **77**, 024027 (2008).

[93] J. G. Baker, M. Campanelli, and C. O. Lousto, Phys. Rev. D **65**, 044001 (2002).

[94] H. Friedrich, Classical Quantum Gravity **13**, 1451 (1996).

[95] M. Alcubierre, *Introduction to* 3 + 1 *Numerical Relativity* (Oxford University Press, Oxford, England, 2008).

[96] N. Bishop, R. Isaacson, R. Gómez, L. Lehner, B. Szilágyi, and J. Winicour, in *Black Holes, Gravitational Radiation and the Universe*, edited by B. Iyer and B. Bhawal (Kluwer, Dordrecht, The Netherlands, 1999), p. 393.

[97] M. Babiuc, B. Szilágyi, I. Hawke, and Y. Zlochower, Classical Quantum Gravity **22**, 5089 (2005).

[98] M. C. Babiuc, N. T. Bishop, B. Szilagyi, and J. Winicour, Phys. Rev. D **79**, 084011 (2009).

[99] N. Bishop and S. Deshingkar, Phys. Rev. D **68**, 024031 (2003).
[100] N. T. Bishop, R. Gómez, L. Lehner, M. Maharaj, and J. Winicour, Phys. Rev. D **60**, 024005 (1999).
[101] E. Berti, V. Cardoso, J. A. González, U. Sperhake, M. D. Hannam, S. Husa, and B. Brügmann, Phys. Rev. D **76**, 064034 (2007).
[102] C. Reisswig and D. Pollney, arXiv:1006.1632 [Classical Quantum Gravity (to be published)].
[103] R. Mönchmeyer, G. Schäfer, E. Müller, and R. Kates, Astron. Astrophys. **246**, 417 (1991).
[104] K. Kotake, S. Yamada, and K. Sato, Phys. Rev. D **68**, 044023 (2003).
[105] S. Yamada, H. Janka, and H. Suzuki, Astron. Astrophys. **344**, 533 (1999).
[106] C. D. Ott, A. Burrows, E. Livne, and R. Walder, Astrophys. J. **600**, 834 (2004).
[107] B. Abbott *et al.* (LIGO Scientific Collaboration), Rep. Prog. Phys. **72**, 076901 (2009).
[108] D. Shoemaker (LIGO Scientific Collaboration), Technical Report No. LIGO-T0900288-v3, 2010.
[109] D. Pollney, C. Reisswig, N. Dorband, E. Schnetter, and P. Diener, Phys. Rev. D **80**, 121502 (2009).
[110] E. Pazos *et al.*, Classical Quantum Gravity **24**, S341 (2007).
[111] E. E. Flanagan and S. A. Hughes, Phys. Rev. D **57**, 4535 (1998).
[112] J. Abadie *et al.* (LIGO and VIRGO Scientific Collaborations), Tech. Report No. LIGO-T0900499-v19, VIR-0171A-10, 2010.
[113] B. J. Owen, Phys. Rev. D **53**, 6749 (1996).
[114] T. Damour, B. R. Iyer, and B. S. Sathyaprakash, Phys. Rev. D **57**, 885 (1998).
[115] B. Abbott *et al.* (LIGO Scientific Collaboration), Phys. Rev. D **73**, 102002 (2006).
[116] B. Zink, E. Schnetter, and M. Tiglio, Phys. Rev. D **77**, 103015 (2008).